GEOSTANDARDS and GEOANALYTICAL RESEARCH

A New Mapping Protocol for Laser Ablation (with Fast-Funnel) Coupled to a Time-of-Flight Mass Spectrometer (LA-FF-ICP-ToF-MS) for the Rapid, Simultaneous Quantification of Multiple Minerals

Dany **Savard***, Sarah **Dare**, L. Paul **Bédard** and Sarah-Jane **Barnes**

LabMaTer, Module des Sciences de la Terre, CERM (Centre d'Études sur les Ressources Minérales), Université du Québec à Chicoutimi, 555 boulevard Université, Chicoutimi, Qc (Canada) G7H 2B1

* Corresponding author. e-mail: ddsavard@uqac.ca

Although *in situ* analysis by LA-ICP-MS is considered a rapid technique with minimal sample preparation and data reduction, mapping areas of millimetres in size using a small beam (< 15 µm) can be time consuming (several hours) when a quadrupole ICP-MS is used. In addition, fully quantitative imaging using internal standardisation by LA-ICP-MS is challenging in samples with more than one mineral phase present due to varying ablation rates. A new protocol for the quantification of multiple coexisting phases, mapped at a rate of about 12 $mm^2 h^{-1}$ and a resolution of 12 µm × 12 µm per pixel, is presented. The protocol allows mapping of most atomic masses, ranging from ^{23}Na to ^{238}U, using a time-of-flight mass spectrometer (ICP-ToF-MS, TOFWERK) connected to a 193 nm excimer laser. A fast-funnel device was successfully used to increase the aerosol transport speed, reducing the time usually required for mapping by a factor of about ten compared with a quadrupole ICP-MS. The lower limits of detection for mid and heavy masses are in the range 0.1–10 µg g^{-1}, allowing determination of trace to ultra-trace elements. The presented protocol is intended to be a routine analytical tool that can provide greater access to the spatial distribution of major and trace elements in geological materials.

Keywords: LA-ICP-MS, LA-ICP-ToF-MS, fast mapping, multiple phases, data reduction.

Received 12 May 22 – Accepted 17 Jan 23

Chemical imaging/mapping at the micro- and nano-scale is growing in popularity and has applications in many fields, such as palaeontology (Pan *et al.* 2019), Earth and planetary sciences (Ubide *et al.* 2015), biology (Theiner *et al.* 2021), environmental science (Moradi *et al.* 2010), archaeology (Selih and van Elteren 2011), and more. Micro-scale chemical composition and variation of major and trace elements in geological materials can record processes involved in mineral formation, deformation, resorption, mobility and alteration (Sylvester and Jackson 2016, Raimondo *et al.* 2017, Neff *et al.* 2020, Chew *et al.* 2021). The abundance of trace elements, and in particular their spatial distribution in minerals, is widely used to trace the source and evolution of ore-forming systems in order to refine petrogenetic models and to develop indicator minerals as tools for exploration of ore deposits (Smythe *et al.* 2008, Dupuis and Beaudoin 2011, Dare *et al.* 2014, Mao *et al.* 2015, Duparc *et al.* 2016, Aulbach *et al.* 2021).

In the field of geology, electron probe microanalysis (EPMA) and micro-XRF are non-destructive methods extensively used for high resolution (1–3 µm beam) mapping of geological samples but both have higher limits of detection compared with LA-ICP-MS (Nadoll and Koenig 2011) and are thus limited to major and minor elemental mapping. LA-ICP-MS is the method of choice to reach sub µg g^{-1} mass fractions of a wide number of elements, and spot or line scan analyses are commonly used for this purpose. Spot or line scan analyses requires only seconds to minutes to acquire data, thus many grains can be sampled in a single specimen. However, this produces individual, spatially isolated data or one-dimensional transects, covering a limited portion of the studied minerals. To better reveal spatial distribution, such as zoning in minerals, exsolution and the distribution of elements among different minerals, 2D chemical mapping by LA-ICP-MS is typically carried out by analysing a series of subsequent line scans (Zhou

doi: 10.1111/ggr.12482

et al. 2017, Duran *et al.* 2020) or a grid of spots (Kelly *et al.* 2017, Neff *et al.* 2020). However, with current instrumentation (discussed below), mapping using LA-ICP-MS is time-consuming and is often restricted to small areas (< 1 mm^2) of the studied polished section.

The duty cycle of Q-ICP-MS limits the data acquisition rate to about 1 to 6 cycles per second (1–6 pixels s^{-1}) under common analytical conditions for mapping, thus limiting the pixel production to this rate. Using a 10-µm beam, an area of 1 mm^2 area (10,000 pixels) can take from 30 min up to 4 h (Lear *et al.* 2012, Lawley *et al.* 2020). Moreover, some ablation cells have long wash-out times, which may result in pixels representing mixed ablation sites. To avoid this phenomenon, a reduced production rate is necessary (Douglas *et al.* 2015). Despite the low pixel production rate, chemical mapping is popular and of growing demand in geoscience as it can reveal incomparable information (Gundlach-Graham and Günther 2016, Sylvester and Jackson 2016).

Achieving fast quantitative chemical images at the micro-scale for the routine determination of both major and trace elements for a wide range of mineral matrices (silicates, sulfides, oxides, phosphates) requires new LA-ICP-MS instrumentation and protocols that fulfil essential requirements. These include: (1) a beam size smaller than the target resolution, (2) a high repetition pulsing rate of the laser (3) a rapid transfer of the aerosol to the ICP-MS to minimise pulse-to-pulse mixing by using a two-volume or a low dispersion ablation cell (Müller *et al.* 2009, Fricker *et al.* 2011) or high efficiency aerosol dispersion cells (Pisonero *et al.* 2006, Wang *et al.* 2013, Gundlach-Graham and Günther 2016, Van Malderen *et al.* 2016), and (4) a rapid analysis of the generated aerosol. The nature of ICP-ToF-MS allows for fast acquisition (33,000 Hz) (Hendriks *et al.* 2017) allowing for the possibility of producing larger maps compared with those generated with a quadrupole ICP-MS (Bussweiler *et al.* 2017, 2020, Neff *et al.* 2020, Chew *et al.* 2021, Savard *et al.* 2021, Van Acker *et al.* 2021). The (quasi-) simultaneous extraction of multiple ion packages in the ICP-ToF-MS instrument allows nearly the full suite of the periodic table to be determined without pre-selecting isotope packages. Extracted ions are accelerated with the same kinetic energy in a flight tube and the travel time of the ions vary as a function of their mass to charge ratio (m/q), with lighter elements hitting the detector first (Myers *et al.* 1994, Borovinskaya 2014). The microchannel plate detector allows about 40,000 times frame detection of each extraction (33,000 Hz) in the ICP-ToF-MS (TOFWERK, TOF-R). Based on its speed only, ICP-ToF-MS has the capacity to produce up to five orders of magnitude more pixels per second compared with ICP-Q-MS. However, because each extraction involves very few atoms, a number of ToF extractions must be summed into each mass spectrum to reach a measurable working signal, which also improves baseline characterisation and subtraction (Hendriks *et al.* 2017). Cumulative extraction also reduces the amount of data to handle. From our experience, a minimum usable bundle of data can be produced in 2 ms (500 Hz) by the summation of sixty-six extractions.

Because large maps are likely to cover multiple phases, a protocol to achieve fully quantitative determination of major and trace elements of multi-phase samples is necessary. Paul *et al.* (2014) proposed an approach based on mineral identification using different strategies, after which, an internal standardisation (IS) method is applied (Longerich *et al.* 1996). A selected element at a fixed mass fraction, determined by microprobe analysis or by assuming stoichiometry values, is fixed for each identified phase. Then, a calibration material is assigned for each phase, again relying on user selection. However, there are several limitations using the internal standardisation method for mapping: a risk of false mineral identification or mineral zonation affecting the internal reference value. Lastly, the mass fraction of the element can be significantly different from stoichiometry since solid solution is common in nature and widespread in composition. Deriving chemistry from the theoretical stoichiometry for these cases may thus lead to false results, loss of information and could render false zonation from homogenously distributed elements. The alternative, acquiring microprobe analyses for multiple phases, is time consuming and expensive. For those reasons, mineral identification from LA-ICP-MS maps can be a useful informative tool but undoubtedly presents risks when used to achieve quantitative mass fractions. An alternative method, which we use in this study, is based on the normalisation of the sum of elements in their oxide form (Liu *et al.* 2008, Selih and van Elteren 2011), except for minerals with no oxygen such as sulfide, to minimise mistakes in mineral identification and to avoid determining a fixed value for an internal standard for each mineral.

Taking into consideration the requirements above, we have developed a new analytical protocol for fast chemical mapping of all atomic masses, ranging between ^{23}Na to ^{238}U, using a time-of-flight mass spectrometer (ICP-ToF-MS, TOFWERK) attached to an 193 nm Excimer laser, equipped with a fast response funnel, that allows quantitative measurement of multiple mineral phases over large areas. The high-resolution maps (12 µm per pixel) are produced at rate of 5 min mm^{-2}. Since mapping by LA-ICP-ToF-MS is quite recent and under development (Burger *et al.* 2017,

Bussweiler *et al.* 2017, Ubide *et al.* 2019, Neff *et al.* 2020, Rubatto *et al.* 2020, Sugiono *et al.* 2022), we detail the optimal analytical parameters required for high-resolution mapping of large areas of thin sections as well as demonstrate that its performance (limits of detection, quality control) is suitable for laser ablation work for various geological applications.

Materials and methods

Instruments and settings

Analytical parameters are summarised in Table 1 and are as follows. A RESOlution 193 nm ArF-Excimer laser ablation system (Applied Spectra, California), used in this study, was attached to an ICP-ToF-MS (Model TOF-R, TOFWERK, Thun, Switzerland) built on a ThermoElemental iCap ICP-Q-MS and recently installed at LabMaTer (Université du Québec à Chicoutimi, UQAC). The laser system was equipped with a large S-155 Laurin Technic double-volume ablation cell and controlled by GeoStar software (Norris Scientific). A rotating slit device was used to shape the laser beam into a rectangular of 12 × 6 µm (length × width) to produce high-resolution chemical maps in this study (see Figure S1 in supplementary material for more details about ablation mode and beam shape). Data were acquired in line-scan mode (overlapping mode) with a fluence of 6 J cm^{-2}, a pulsing rate of 120 Hz, and a beam displacement speed set to 360 µm s^{-1}. In addition, a small-volume fast-response funnel (FRF) device (Norris Scientific and Laurin Technic) was attached to the laser to ensure rapid transfer of the ablated aerosol out of the ablation cell and through the transfer tubing to the ICP-ToF-MS. The mapping production rate was 30 pixels s^{-1}, allowing an area of 10 mm^2 to be mapped in 45 min. The fast-response funnel works under positive pressure (~ 25 kPa) and the S-155 ablation cell was flooded with 1000 ml min^{-1} of helium mixed with 400 ml min^{-1} of argon in the FRF cup. An additional 300 ml min^{-1} auxiliary argon flux was injected into the gas mixture at the torch of the ICP-ToF-MS. To avoid detector saturation and reduce background noise (H_2O^+, $^{16}O^+$, $^{18}O^+$, $^{14}N^+$, $^{12}C^+$), a low-mass cut-off was applied using ThermoElemental QCell technology by setting the collision/reaction cell (CRC) mass and bias voltages to +230.5 V and +0.97 V respectively. Although, Burger *et al.* (2019), demonstrated that the injection of H_2 and He into the reaction/collision cell can noticeably reduce $^{40}Ar^+$ and $^{80}ArAr^+$ interferences and improve selenium detection, no reaction/collision gas nor any N_2 was added to the gas mixture in our experiment. After testing different optional gas mixtures (N_2/H_2/He) in our system, it was concluded that the benefits of reducing polyatomic interferences were less than the formation of polyatomic MH^+ and oxides that formed when adding any gas. Four notch filters are available on the instrument and are RF-only quadrupole to which four auxiliary RF frequencies can be applied to selectively attenuate ions of specific *m/z* in ICP-ToF-MS (Hendriks *et al.* 2017). The RF filters were set to reduce signal on masses ^{40}Ar, $^{80}ArAr^+$, ^{56}Fe and ^{63}Cu and avoid detector saturation while analysing Fe-sulfides, Fe-oxides, chalcopyrite, and the reference material (RM) MASS-1 (Fe-Cu-Zn sulfide).

Table 1.
List of analytical parameters used for the LA-ICP-ToF mass spectrometry

Parameter	Value
Beam size	6 µm × 12 µm
Pulsing	120 Hz
Fluence	6 J cm^{-2}
Displacement speed	360 µm s^{-1}
He flow (cell)	1000 ml min^{-1}
Argon (cell)	400 ml min^{-1}
Argon (additional)	300 ml min^{-1}
CRC additional gas	None
CRC mass voltage	+230.5 V
CRC bias voltage	+0.97 V
Cumulative extractions (ToF)	1100
Scanning time	33.3 ms
Wash-out time (FW0.01M)	44 ms
Wash-out time (FW0.03M)	33.3 ms
Notch filter mass	40, 56, 63, 80
Pixel production rate	30 pixels s^{-1}
Mapping size	2 mm × 5 mm
Mapped area	10 mm^2
Total time	46 min
Total pixels	70140
Isotope selection	^{107}Ag, ^{27}Al, ^{75}As, ^{197}Au, ^{137}Ba, ^{209}Bi, ^{44}Ca, ^{111}Cd, ^{140}Ce, ^{59}Co, ^{53}Cr, ^{133}Cs, ^{65}Cu, ^{163}Dy, ^{166}Er, ^{153}Eu, ^{56}Fe, ^{71}Ga, ^{157}Gd, ^{73}Ge, ^{178}Hf, ^{202}Hg, ^{165}Ho, ^{115}In, ^{193}Ir, ^{39}K, ^{139}La, ^{175}Lu, ^{24}Mg, ^{55}Mn, ^{95}Mo, ^{23}Na, ^{93}Nb, ^{146}Nd, ^{60}Ni, ^{189}Os, ^{31}P, ^{208}Pb, ^{105}Pd, ^{141}Pr, ^{195}Pt, ^{85}Rb, ^{185}Re, ^{103}Rh, ^{101}Ru, ^{34}S, ^{121}Sb, ^{77}Se, ^{28}Si, ^{147}Sm, ^{118}Sn, ^{88}Sr, ^{181}Ta, ^{159}Tb, ^{125}Te, ^{232}Th, ^{47}Ti, ^{205}Tl, ^{169}Tm, ^{238}U, ^{51}V, ^{182}W, ^{89}Y, ^{172}Yb, ^{66}Zn, ^{90}Zr

The instrument tuning was achieved with NIST SRM 610 glass and GSE-1G (USGS basaltic glass), and the formation of interferences was verified on the mean ion detection of the mapped sample (HN99-46) using the TofDAQ Viewer software (TOFWERK). Oxide and hydroxide interferences were monitored from $^{248}ThO^+/^{232}Th^+$ and $^{249}ThOH^+/^{232}Th^+$ and were < 1%. Double-charged species were monitored from $^{141}Pr^{2+}/^{141}Pr^+$ and $^{181}Ta^{2+}/^{181}Ta^+$ and were < 0.5%. Background on the

gas blank was ~ 1 Mcps (~ 31 ions per extraction) on the entire mass spectrum, dominated by peak and tailing on masses 18 (H_2O), 28 (Si^+), 36 (Ar^+), 32 (O_2^+), 56 (ArO^+) and 54 (ArN^+). Using the 12 × 6 µm beam, total cps were about 1.5 Mcps and 3.0 Mcps on NIST SRM 612 and NIST SRM 610 respectively with a resolution from ~ 2500 (m/Δm) on ^{238}U to ~ 2000 (m/Δm) on ^{23}Na. Isotope precision was assessed from $^{153}Eu/^{151}Eu$ on NIST SRM 610 over a 10-s integration period and was 4.4% RSD. Sensitivity on heavy and mid masses (^{238}U and ^{165}Ho) was similar, about 160 cps per µg g^{-1} and 150 cps per µg g^{-1} respectively, and much lower for light masses being at 0.7 cps per µg g^{-1} (^{28}Si). A total of 107 isotopes from sixty-six elements were treated. Multiple isotopes were acquired for many elements, thus noticeably increasing the quality control of potential interferences. In the interests of brevity, concentrations from a single selected isotope per element (sixty-six in total, Table 1) are presented here but complete data sets are available upon request. To help evaluate the quality control of minerals from the studied sample (HN99-46), SEM analyses were conducted at IOS Services Géoscientifiques (Canada) using a Zeiss Sigma 300 VP field emission scanning electron microscope (FE-SEM) equipped with two Oxford Instruments 170 mm^2 Ultim-Max EDS-SDD. The acceleration voltage was set to 20 kV and an aperture of 30 µm at high current was used to obtain sufficient counts in the EDS detectors with a dead time lower than 40%.

Pixel production rate

The effective wash-out time using specific analytical parameters and instrument set-up was evaluated to optimise the pixel production rate. Both transport speed and efficiency of the aerosol from the ablated site to the ICP-MS are essential to achieve fast mapping at the micrometre level (Van Malderen *et al.* 2015, 2016). The wash-out time, which is defined as the time required for the ablated aerosol to be swept out of the ablation cell and through the transfer tubing (Gundlach-Graham and Günther 2016), is commonly expressed as the time required to reach 1% of the remaining signal (99% wash-out) and noted as full-width at 1% maximum (FW0.01M), compared with its reference maximum peak intensity after a single laser shot (see Figure 1a). As a rule of thumb, the faster the wash-out, the higher the pixel production rate can be achieved when coupled to a fast measurement instrument such as ICP-ToF-MS. A longer wash-out time than the pixel production rate may result in undesirable tailing (memory) effects on the images when running continuous line scan analyses to produce maps. On the other hand, a lower pixel production rate would not take full advantage of the high speed of

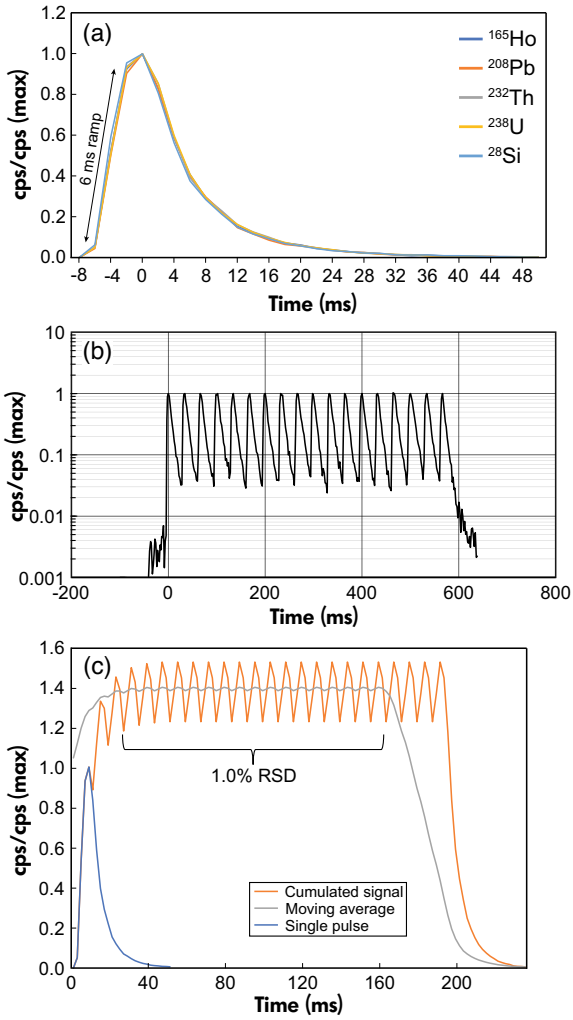

Figure 1. (a) Wash-out of the fast response funnel (Norris Scientific and Laurin Technic) as tested at LabMaTer, mean of thirty individual laser pulses on NIST SRM 610, for U, Th, Ho, Pb and Si, using a 12 × 6 µm beam, 6 J cm^{-2}. (b) 30 Hz laser pulsing on GSE-1G: Mean ^{28}Si, ^{165}Ho, ^{208}Pb, ^{232}Th and ^{238}U of response wash-out using a 12 µm × 6 µm beam on GSE-1G. Peak was resolved to FW0.03M level (±97% wash-out). (c) Simulation of pulsing oscillation. The blue line is the actual response of a single pulse (data from Figure 2). The orange line is the simulation of the actual wash-out efficiency of the fast-response funnel at 120 Hz laser frequency at 2 ms reading interval, and the grey line is the theoretical moving average from four laser pulse (33.3 ms) integrations showing a negligible variation of 1.0% RSD (2*s*).

ICP-ToF-MS. "Small volume dispersion cells" have been recently improved to decrease the wash-out time to milliseconds (Van Acker *et al.* 2021, Van Malderen

et al. 2016), and are referred to as "fast-response-funnels" (FRF). The performance of the Norris Scientific/Laurin Technic FRF used on our laser system was evaluated to optimise the pulsing rate and the beam displacement. The wash-out efficiency greatly depends on the design of the funnel (Gundlach-Graham and Günther 2016, Van Malderen *et al.* 2016). The effective wash-out time also varies according to: (1) the total amount of aerosol generated by the single-pulse laser, (2) the nature of the elements (volatile versus non-volatile), (3) the isotopic abundance, (4) the mass fraction of the element and (5) the sensitivity of the instrument at the measured mass. For instance, Burger *et al.* (2017) reported a FW0.01M achieved after 100 ms when using a 44 μm beam while it was reduced down to < 10 ms when using a 5 μm beam. Comparing wash-out times without using identical analytical parameters, materials and instrument settings is thus meaningless and only serves as a crude indicator of the cell potential.

Without the use of the fast-response funnel, the wash-out time of the S-155 cell (Laurin Technic) used in this work was measured at about 420 ms to reach FW0.01M, while it was about ten times faster when using the fast-response funnel (Norris Scientific and Laurin Technic). Using the analytical conditions of the present work (Table 1), we find wash-out times of about 38 ms at FW0.01M and 56 ms at FW0.001M based on an average of the signal from ^{238}U, ^{232}Th, ^{208}Pb, ^{165}Ho and ^{28}Si from thirty individual pulses on NIST SRM 610 (Figure 1a). As shown on Figure 1a, about 6 ms was necessary before the signal reaches the maximum peak. This 6 ms "ramp" should also be considered; thus, the whole event is 44 ms and the ideal acquisition frequency would be 1/0.044 s (= 23 pixels s^{-1}). Our results show that a production rate of about 30 pixels per second would be realistic considering that the ablation cell could be washed out to FW0.03M at about that frequency. To verify the efficiency of the fast response funnel, a sequence of 30 Hz pulsing was carried out on GSE-1G. The wash-out between each pulse was about 97% for GSE-1G (FW0.03M, Figure 1b), confirming that a pixel production rate of 30 Hz would be suited to minimise the risk of producing artefact tailing from the wash-out and optimising the production rate.

To produce pixels of square shape, both the stage translation and data production rate must be synchronised with the pixel target production rate, here established at 30 Hz. The data acquisition was thus set to 30 Hz by the integration of 1100 extractions (33,000 Hz instrument frequency extractions / 30 Hz target frequency pixel production) for a total of 33.33 ms of cumulative integration time for each point of data. The pixel width was determined by the beam vertical length, here 12 μm, thus the stage displacement speed was fixed to 360 μm s^{-1} (30 Hz × 12 μm = 360 μm s^{-1}).

While a pulsing effect from the combined oscillating aerosol flow and scan period of sequential quadrupole ICP-MS measurement may lead to aliasing (pulsed / frequency) error (Hattendorf *et al.* 2019, Norris *et al.* 2021), this undesirable effect is partially resolved by the simultaneous acquisition nature of ICP-ToF-MS. However, signal pulsing could occur from the oscillating aerosol flow, thus a quasi-stationary mass flow to the ICP-MS should minimise this effect (Hattendorf *et al.* 2019, Norris *et al.* 2021). The constancy of the material flow was optimised by using a pulse frequency of 120 Hz on the laser. At this rate, a pulse occurs each 8.3 ms leading to a wash-out of about 16% (FW0.84M) between pulses. Consequently, aerosol clouds from the pulses are mixed and no obvious pulsing effect was observed. A simulation was carried out using a 120 Hz pulse rate (Figure 1c) of the laser based on the measured wash-out of a true single test run on NIST SRM 610 (Figure 1a). It shows that an oscillation of the signal is present when averaging the integrated signal summed over four pulses of the laser; however, the theoretical relative deviation on the mean is negligible at 1.0% (2*s*). The analysed material generated from the equivalent of four laser pulses is thus accumulated over the 33.3 ms integration period of the ICP-ToF-MS, producing individual pixels with minimum potential for the pulsing effect. The cumulative pulses also improve the signal to noise ratio and reduce the measurement uncertainty compared with pulse-to-pulse mode (Neff *et al.* 2020, van Elteren *et al.* 2021).

Calibration material

Best practice in LA-ICP-MS recommends the use of matrix-matched reference materials (RM) for the primary calibration (Longerich *et al.* 1996, Sanborn and Telmer 2003, Danyushevsky *et al.* 2011, Sylvester and Jackson 2016) or as secondary calibrants to account for matrix effects (Gilbert *et al.* 2013, Thompson *et al.* 2021a, b). A total of six reference materials were used for the new multi-phase calibration method to allow quantification of a wide range of minerals (silicates, oxides, sulfides, phosphates and carbonates). The main block of calibration consisted of three glasses (NIST SRM 610, GSE-1G, GSD-1G) and two sulfides (MASS-1 and UQAC-FeS-1). UQAC-FeS-1 is a nano-powdered pressed pellet developed at LabMaTer (Savard *et al.* 2018) of a natural Fe(Ni-Cu)-sulfide from Ragland nickel mine (Katinniq, Quebec) and doped with chalcophile elements, including PGE, fused in a carbon crucible and then crushed to a nano-powder and pressed into pellets of 13 mm

diameter using a technique described in Garbe-Schönberg and Müller (2014). A natural apatite from Durango (Lyons 1988, Chew *et al.* 2016) was also used for the specific calibration of P because the glasses used for calibration only contain a few μg g^{-1} of P. As underlined by Cook *et al.* (2016), NIST SRM 610 is best suited for silicates, while GSE-1G and GSD-1G were used with success as calibrants (primary/secondary) and for quality control of Fe-oxides, (Savard *et al.* 2012, Dare *et al.* 2014, Duran *et al.* 2020), chromite (Arguin *et al.* 2016), ilmenite (Thompson *et al.* 2021b), olivine (Batanova *et al.* 2019), garnet (Guilmette *et al.* 2018) and sulfides (Duran *et al.* 2019, Lawley *et al.* 2020). NIST SRM 610 can also be used for carbonates, such as otoliths (Lazartigues *et al.* 2014, Jochum *et al.* 2019, Thompson *et al.* 2021a). Finally, MASS-1 and UQAC-FeS-1 are both suited for LA-ICP-MS analysis of sulfide minerals (Wilson *et al.* 2002, Danyushevsky *et al.* 2011, Duran *et al.* 2019, Lawley *et al.* 2020, Andronikov *et al.* 2021). Calibration using a variety of matrix RMs has the advantage of producing an extended coverage of the elements because no single reference material can cover all (see online supporting information Table S1). For example, S, Te, Se, Pt, Pd, Os, Ir, Au are noticeably present in higher mass fractions and are better characterised by the sulfide RM compared with the glass RM.

Quality control reference material (QCRM)

In addition to the six RMs used for calibration, sixteen QCRMs were analysed to extend the evaluation of the accuracy of the new calibration protocol for a wide variety of matrices. These include three glasses (G-Probe-15, NIST SRM 612 and NIST SRM 614), a synthetic sulfide doped with PGE and Au (PO-727, Memorial University), a series of natural minerals (see Table S1 for details) and a series of nano-powder pressed pellets prepared at LabMaTer using a Planetary Mill and following the method of Garbe-Schönberg and Müller (2014). These comprise powders of a high purity concentrate of natural apatite (UQAC-APA-1) from Lac-à-Paul Ti-P deposit (Arianne Phosphate, Quebec), an ilmenite-rich sand (AMIS-0454), a natural otolith (in-house RM under development) and three sulfides (PTC-1b and CCu-1e from CCRMP; UQAC-FeS-5, an in-house RM under development at LabMaTer (Savard *et al.* 2018)). A full description of reference materials is provided in Table S1 and the measurement results for the quality control RMs are given in Table S2.

Data reduction

Post-acquisition data processing of ToF data required two steps. The raw data (h5 format) were first treated in Tofware software (TOFWERK) to select isotopes, refine the peak (shape, position, width) and proceed to baseline subtraction (Hendriks *et al.* 2017). The modified h5 files were then loaded in IOLITE v4 software (Paton *et al.* 2011) where a new data reduction scheme, the "3D Trace Elements" (3D-TE-DRS) was, in part, developed in cooperation with the IOLITE team during this study in order to convert the raw data to quantitative multi-mineral maps. The 3D-TE-DRS can combine multiple RMs and produce blocks of calibration over time. The normalisation to 100% weight method was used, which has been proven to work well for RM synthetic glasses (Gagnon *et al.* 2008, Liu *et al.* 2008). For the calibration, the median of common isotopes of each RM were normalised to GSE-1G and the linear sensitivity were all forced to the origin.

In the new 3D-TE-DRS, each individually acquired datum (pixel) in the map can be attributed to a mineral phase based on the signal detection in the instrument from user-selected elements and using threshold or gap limits (< or > larger or less than) from as many elements as necessary. For example, sulfide and apatite can be easily identified using the detection threshold signal (> × cps) of ^{34}S and ^{31}P respectively, whereas differentiating silicate phases, such as amphibole and pyroxene, will require different threshold or gaps from the same elements. Minor elements can also be of help to refine the identification. An appropriate element oxide form is then applied based on the phase attribution. When a sulfide is recognised, oxygen is excluded from the normalisation. Also, as Fe occurs in various oxidation states, such as Fe^{2+} in ilmenite, Fe^{3+} in haematite and a combination of Fe^{2+} and Fe^{3+} in magnetite (equivalent of ~ Fe_3O_4), the appropriate oxide conversion is applied according to mineral identification based on the chemical criteria set by the users. Finally, an appropriate sum for the normalisation is applied to each identified phase and can differ from 100% to compensate for any major component that cannot be detected by LA-ICP-MS, such as CO_2, OH, H_2O and the halogens (F, Cl, Br, I). For most anhydrous or volatile-free minerals, the normalisation will be forced to 100%, while calcite, which contains 44% CO_2, normalisation was forced to 56%. Having the flexibility to adjust the normalisation protocol for each identified pixel is only now possible using the new IOLITE 3D-TE-DRS.

Analysed sample

To demonstrate the versatility of the new mapping protocol, a sample (HN99-46, Figure 2) of magmatic Fe-Ti-P mineralisation from the Critical Zone of Sept-Iles layered intrusion, Quebec, Canada (Nabil 2003, Tollari *et al.* 2008) containing a diversity of mineral phases (oxides, phosphate,

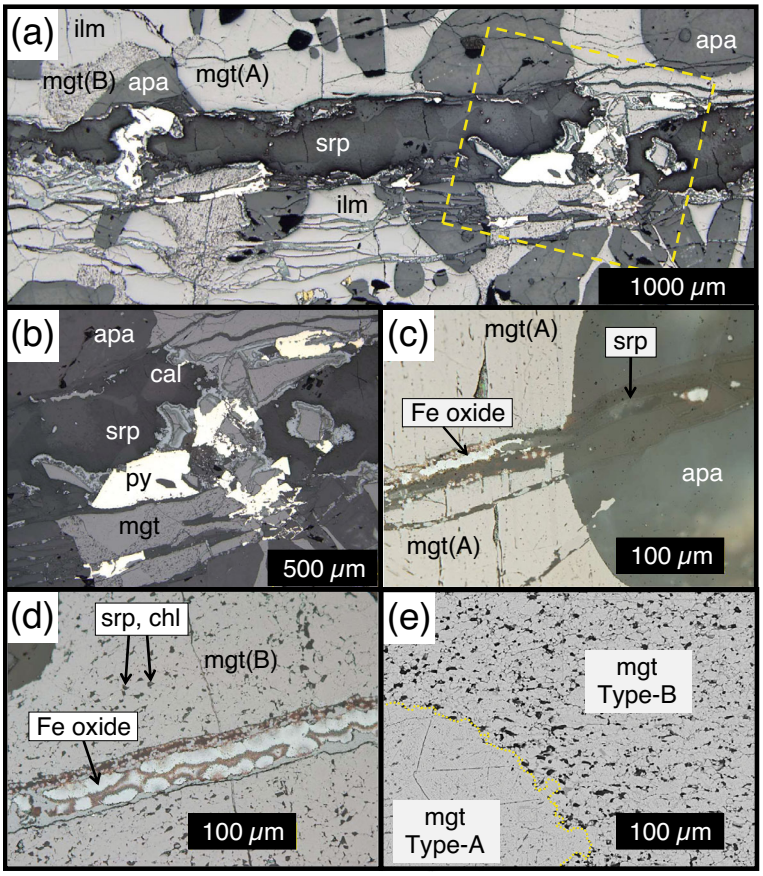

Figure 2. Reflected light images of Fe-Ti-P mineralisation (sample HN99-46, 100 μm thick section) from Sept-Iles layered intrusion, Quebec. (a) Mapped area (2 mm × 5 mm) showing a late-stage vein cross-cutting the igneous assemblage of apatite, ilmenite and titanomagnetite. (b) Close-up image of the pyrite grain in late-stage serpentine vein showing complex mineral relations (yellow dashed box from 5a). (c, d) Complex network of micro-veins cross-cutting resulting in alteration of magnetite (type-B). (e) SEM images of titanomagnetite: unaltered "Type-A" with distinctive ilmenite exsolution lamellae and few inclusions, "Type-B" alteration of titanomagnetite hosting inclusions of chlorite and serpentine of < 15 μm in size. Apatite (apa), calcite (cal), serpentine (srp), pyrite (py), titanomagnetite (mgt), chlorite (chl).

sulfide, carbonate and silicates) was used to produce a 2 mm × 5 mm map. The mineralised sample is dominated by igneous apatite, coarse-grained ilmenite, and titanomagnetite (type-A) containing very fine exsolution of ilmenite (Figure 2e). In order to demonstrate the high-resolution of the new mapping protocol, the 2 mm × 5 mm mapped area was chosen to include fine-scaled features, such as a late-stage vein of serpentine with calcite and pyrite (Figure 2a). A close-up image of pyrite in the mapped area is provided in Figure 2b. Thinner veinlets of serpentine and magnetite (Figure 2c, d) also cross-cut titanomagnetite and apatite. Titanomagnetite, near this late-stage vein, is partially altered (type-B) and contains small inclusions (< 15 μm) of serpentine and chlorite as identified by SEM. The H_2O content (20%) of serpentine in the vein was calculated using SEM analysis (at IOS Services Geoscientifiques, Chicoutimi) and the normalisation was therefore forced to 80%.

Results and discussion

Since this is one of the first applications of laser ablation mapping of geological samples using ICP-ToF-MS, emphasis is placed on evaluating the method performance and figures of merit regarding limits of detection and quality of the data. In addition to using "external" reference materials to evaluate the quality of the data, fully quantitative data extracted from the mapped area of the different phases is directly compared with data obtained by traditional means from previous work (by LA-ICP-MS, EPMA) and this study

(SEM analysis). The partitioning behaviour of trace elements for the minerals also supports the evaluation. The advantages and limits of the method are highlighted by the analytical capabilities in the geochemical context of the project presented here.

Limits of detection

Both a lower limit of detection (LLoD) and an upper limit of detection (ULoD) specific to the method must be calculated because of the limited linearity of ICP-ToF-MS. The peak tailing effect on adjacent masses, combined with overlapping peak shapes and stray ions, produce a mass-spectral baseline that requires post-acquisition peak fitting and baseline subtraction (Figure 3). This ICP-ToF-MS baseline is known to have negative effects on the sensitivity and the stability of the signal for important elements in geology, such as B, Li and K (Hendriks *et al.* 2017, Gundlach-Graham *et al.* 2018). In addition, approaching detector saturation affects the linearity of the instrument (Hendriks *et al.* 2017) and can occur in two different ways: (1) the signal on a single mass exceeds 10 Mcps (> 300 ions detection per extraction) and (2) the signal of the entire mass spectrum exceeds 30 Mcps (> 900 ions detection per extraction). Reducing the sensitivity of the light-mass elements (^{23}Na to about ^{75}As) significantly increases their lower limits of detection (LLoD), but since many minerals of interest are composed of light mass atoms as major components (calcite, magnetite, pyrite, apatite, etc.), working with higher LLoD in this mass range has only a moderate negative impact on the results.

The LLoD were calculated on the baseline instead of the gas blank, since this represents more realistic values for ICP-ToF-spectrometry, as demonstrated by Thompson *et al.* (2020). The ULoD were estimated from the sensitivity (ions per extraction per µg g^{-1}) of each element, assuming saturation occurs on individual peaks at 300 ions detection per extraction. For light masses ranging between ^{23}Na and ^{75}As, detector saturation should not be possible under the analytical conditions used here. However, for heavy masses, noticeably ^{238}U, ^{232}Th, ^{205}Tl, ^{181}Ta, ^{209}Bi, ^{175}Lu and ^{169}Tm, saturation could occur between 5–10% *m/m*. The broad detector saturation, which can occur from the whole spectrum at 30 Mcps, was not considered in the estimation of the ULoD. Both LLoD and ULoD, using analytical parameters used for mapping (12 µm × 6 µm beam), are provided (Table S3) and are summarised in Figure 4. The LLoD for elements < 85 amu (^{23}Na to ^{85}Rb) generally range from 15–350 µg g^{-1}, with the highest LLoD at 2500 µg g^{-1} (^{34}S). LLoD for elements > 85(Rb) masses generally range between 0.15 to 5 µg g^{-1}, with the lower values ranging between 0.11 and 0.15 µg g^{-1} for U, Th, Tl and Ta. This significant difference in LLoD between the light masses and mid-heavy masses is due, in part, to the reduced sensitivity applied by the low-mass cut-off setting on the Qcell. The negative impact of the higher LLoD for light masses is minimal for many minerals, whereas elements of mid-heavy masses (REE and most transition metals) commonly occur as minor to ultra-trace mass fractions and thus require much lower LLoD. Low levels of U and Th (< 0.12 µg g^{-1}) can potentially be measured in a very small volume of sample. We evaluated that each laser pulse was removing

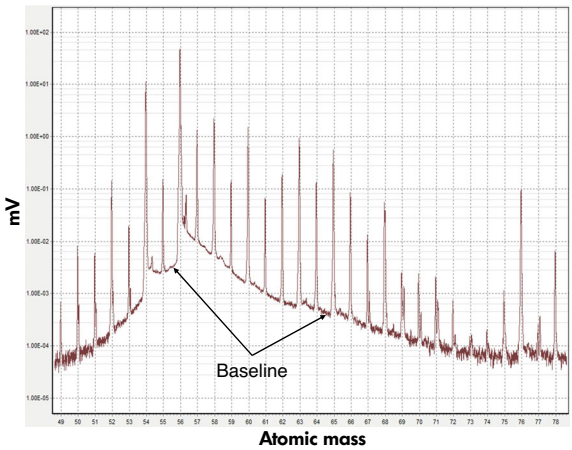

Figure 3. Example of an ICP-ToF-MS baseline and peak (from a cumulated spectrum).

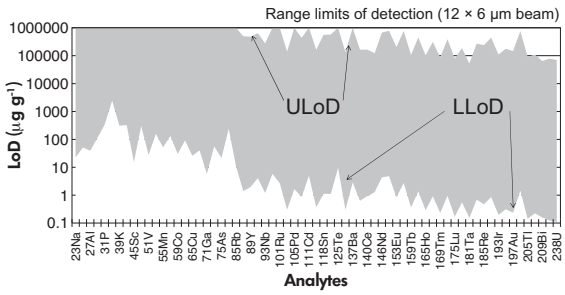

Figure 4. The range of limits of detection (Upper LoD (ULoD) and Lower LoD (LLoD)) provides an estimation of the workable mass fractions of the presented mapping protocol using a 12 µm × 6 µm beam (rectangle) as calculated from the baseline of the ICP-ToF-MS. The upper limit of detection (ULoD) being higher than 100% *m/m* for amu < 75, detector saturation should not occur for those low atomic number ("light") elements.

about 0.1 μm of material, and the integration of four laser pulses (12 × 6 μm beam) used to produce each pixel of data would thus remove a volume of about 28.8 μm^3 of material. Assuming a density of a mineral being about 3.5 g cm^{-3}, the integrated mass sample per pixel equivalent is 1 × 10^{-10} g (100 pg) and the total amount of U and Th potentially detected in this sample is 1.2 × 10^{-17} g (0.012 fg), which is about two orders of magnitude lower that the limits of detection reported elsewhere based on a test portion of 4 μg of material (Macholdt *et al.* 2014).

The effective linear dynamic range for light masses for the method are as low as three to four orders of magnitude, whereas it is generally six orders of magnitude for the mid and heavy masses. These observations are in good agreement with previously reported performance of the ICP-ToF-MS (Bleiner *et al.* 2000, Tanner and Günther 2008, Hendriks *et al.* 2017). As a consequence, the determination of trace elements (< 10 μg g^{-1}) in the light mass range (< ^{85}Rb, with the exception of Ga) is not possible with the instrument settings used. Also, the detector saturation can be, in some cases, a limiting factor in terms of flexibility in mapping analysis of multiple mineral phases. Minerals with major elements having multiple isotopes of high abundance, such as Pb (208, 207 and 206), would make it impossible to 'notch' all three main isotopes and thus would make the analysis of minerals, such as galena (PbS), impossible as saturation is expected to occur at about 11% *m/m*, comparable to an experiment conducted by Gundlach-Graham *et al.* (2018) using a 5 μm beam. The same issue is expected to occur for platinum-group minerals and alloys, and REE-rich phases. On the other hand, the analysis of minerals for which major elements are mono-isotopic or are dominated by a single isotope, such as uraninite (UO_2) with ^{238}U (natural abundance of 99.3%), pyrochlore [$(Na, Ca)_2Nb_2O_6(OH,F)$] with mono-isotopic ^{93}Nb and arsenopyrite (FeAsS), might be possible if the notch on ^{63}Cu is switched to ^{238}U, ^{93}Nb or ^{75}As respectively. This implies that these minerals could be analysed only under specific notch filter tuning.

LLoD comparison with LA-ICP-Q-MS

Compared with single-quadrupole ICP-MS, time-of-flight spectrometers have lower sensitivity in solution mode (Hendriks *et al.* 2017). To compare the LLoD with ICP-Q-MS (see results in Figure 5), the laser was attached to an Agilent 7900 ICP-Q-MS using the same laser settings. However, the fast-funnel was not used since the wash-out time is too fast for the acquisition time of the ICP-Q-MS. A total of fifty-five isotopes were pre-selected and a dwell time of 5 ms was set to each mass for a total sweep time of 0.377s per cycle. ^{44}Ca was used as the internal standard element and the LLoD as obtained from the USGS basaltic glass GSE-1G was used for the comparison, thus data are missing for ^{34}S, ^{77}Se and the PGE. Except for ^{28}Si, which has comparable LLoD in both instruments, the LA-ICP-ToF-MS LLoD are typically higher for the light masses by a factor of about 10 to 1000 (Figure 5), in agreement with Hendriks *et al.* (2017). For elements with heavier masses (between ^{107}Ag and ^{195}Pt) the LLoD are only 10× higher by ToF

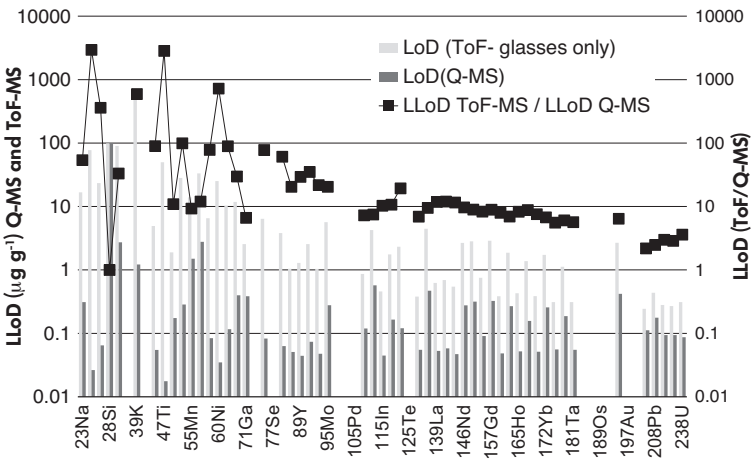

Figure 5. LLoD comparison between LA-ICP-ToF-MS with a fast funnel (light grey bars) and LA-ICP-Q-MS without the fast funnel (dark grey bars) from GSE-1G (USGS). The axis on the left shows the LLoD μg g^{-1} ranges and the axis on the right compares the LLoD from ICP-ToF-MS and ICP-Q-MS as proportions (black squares).

compared with quadrupole and for masses ^{205}Tl to ^{238}U the LLoD are 5× higher by ToF-MS. The detailed data are provided in Table S3.

It should be noted however that acquiring data in such conditions by ICP-Q-MS would not be possible for mapping. The sweep time of ICP-Q-MS, being 0.377 s, would limit the pixel production rate to less than 3 pixels s^{-1}. With a displacement speed of 360 µm s^{-1}, each pixel would have been about 120 µm wide. To produce a 12-µm wide pixel, the beam displacement speed should be set to 36 µm s^{-1} instead of 360 µm s^{-1}. In doing so, the cumulated pulses would have been forty instead of four to produce one pixel. Assuming that the ablation rate is about 0.1 to 0.3 µm per pulse, cumulating forty pulses would have produced a laser trench of about 4 to 12 µm depth. At such a depth, the angle of ablation would be very steep and the material ejection from the plume at the impact site would be oblique (Conde *et al.* 2004). Therefore, a true effective comparison between ICP-Q-MS and ICP-ToF-MS is not possible as the trade-off of the apparent lower sensitivity of the ICP-ToF-MS is counterbalanced by the effective, fast data acquisition.

Quality control

Reference materials: Comparisons of results for reference materials with working values are shown in Figures 6, 7 and 8, and the statistics are provided in Table 2. Mass fractions below LLoD were removed and the data set comprised 605 measurement results, averaged from two measurements from a total of twenty-two reference materials. Detailed results are provided in Table S2. Analytical conditions were the same for the RMs as for the mapping experiment (Table 1). It should be noted that some analyses were as short as 0.5 to 2.5 s because the speed of beam displacement (360 µm s^{-1}) covered rapidly the small grains (< 1 mm) of natural minerals, such as the Madagascar apatite, Laflamme PO-727 sulfide, chromite CHR-M1a, R-10 rutile, and the Mongolian Olivine (sh11-2). Furthermore, the natural minerals may have heterogeneities, thus resulting in large uncertainties in the working values (Eggins and Shelley 2002, Danyushevsky *et al.* 2011, Gilbert *et al.* 2013, Batanova *et al.* 2019, Thompson *et al.* 2021a) and/or there could be low confidence in the working values resulting from challenging elements and matrices. Therefore, we propose a simplified approach in order to track systematic problems that could increase the risk of false measurement on the unknown samples.

In Figure 6, the results from the analysed RMs are compared with their working values according to the following

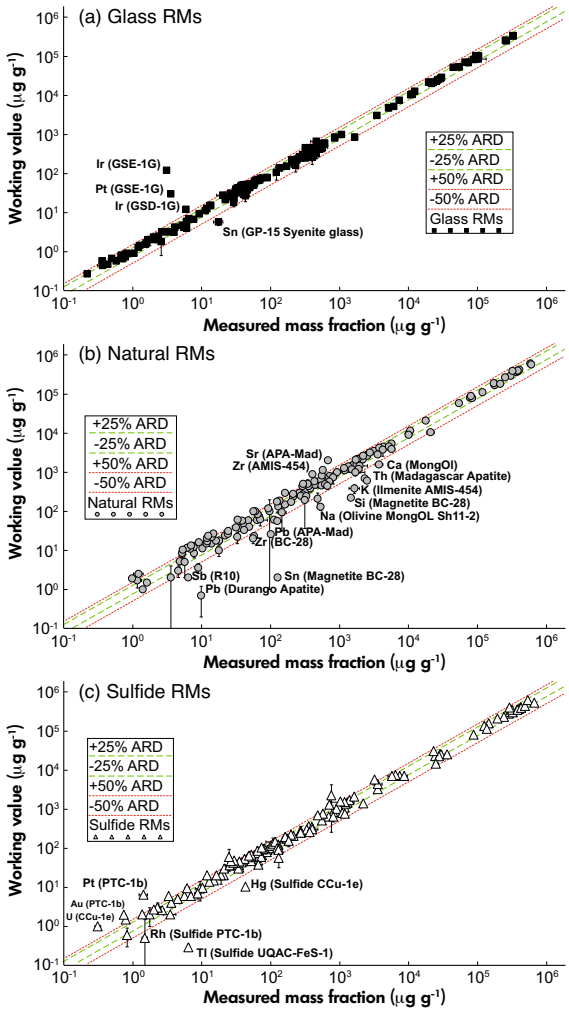

Figure 6. Quality control for all reference materials using the new mapping protocol (12 µm × 6 µm beam, 360 µm s^{-1}). Comparison of the working values and measured values for (a) glass RMs, (b) natural RMs and (c) sulfide RMs. Some element outliers are identified on the graphs, more details are provided in the discussion section and the complete data set is provided in Table S2.

three categories: glass RMs, natural RMs and sulfide RMs. For each datum (i), an absolute relative difference (ARD%) was calculated by comparing measured values (m_i) with their working value (WV_i) from the following equation:

$$ARD = \left| \frac{WV_i}{m_i} - 1 \right| x100 \qquad (1)$$

For clarity and simplification, each datum is subdivided into three classes based on their ARD(%): data with less than 25% ARD are considered as acceptable. This threshold is based on the relative uncertainties (*U*) of both the reference

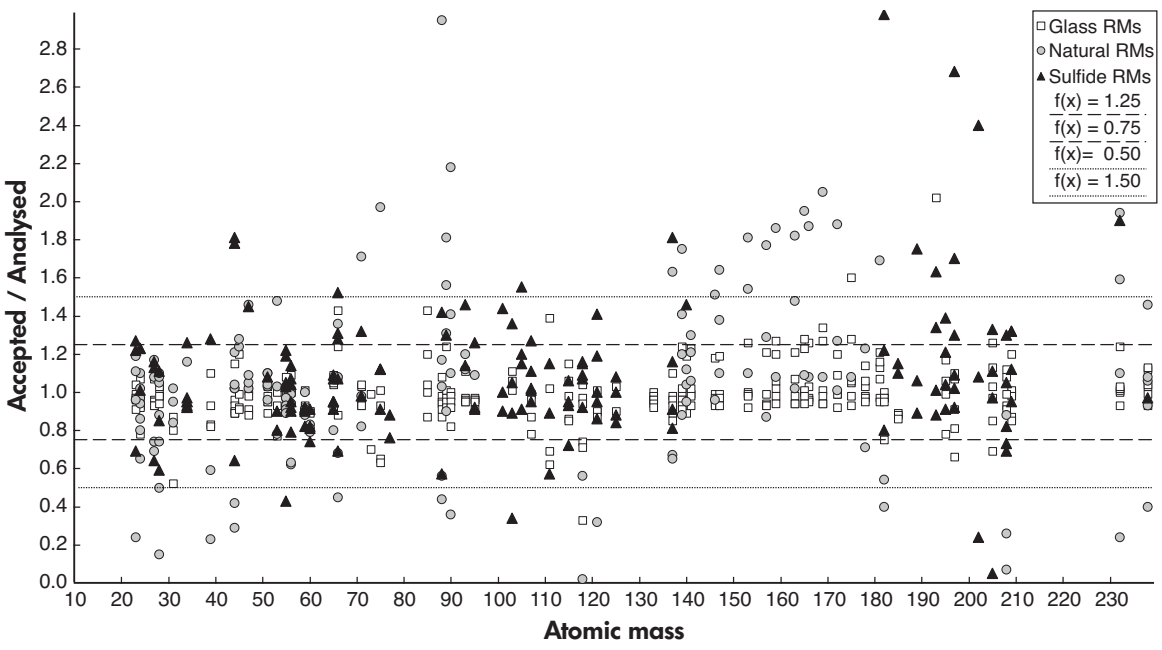

Figure 7. Quality assessment of reference materials (RM) for the three types (glass, natural and sulfide) as a function of atomic mass. The dotted lines are 25% and 50% ARD.

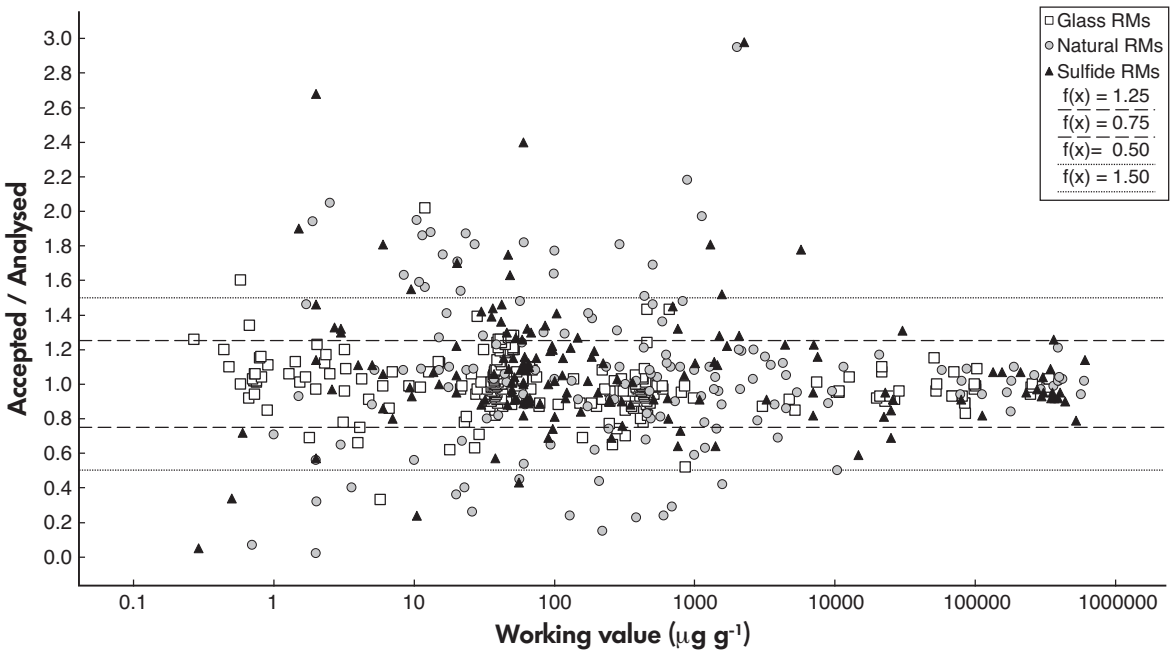

Figure 8. Comparison of the measured absolute relative difference (ARD%) with working values in the reference materials (RMs). The dotted lines are 25% and 50% ARD.

material and the analytical uncertainties which were trivially estimated at 15% and 20% (RSD%) respectively for all RMs, and cumulated by the equation $U_{Budget}^2 = (U_{RM}^2 + U_{Measurement}^2)$. A second level was set for data ranging between 25% and 50% of ARD to the working values. The data mostly plot close to the accepted values (Figure 6), however, users should be aware that the occurrence of low-quality results is possible. Finally, data with > 50% ARD of

Table 2.
Compilation of the quality control reference materials (RMs), comparing the absolute relative difference (ARD%) from the working values (WV) of a total of 605 results from twenty-two reference materials analysed using the new mapping protocol

	Glass RMs	Natural RMs	Sulfide RMs	Total
TOTAL data	294	152	159	605
< 25% ARD with WV	268	87	107	462
Proportion	91%	57%	67%	76%
25% to 50% ARD with WV	21	27	34	82
Proportion	7%	18%	21%	14%
> 50% ARD with WV	5	37	18	60
Proportion	2%	24%	11%	10%

See Table S1 for the list of reference materials.

the working values are flagged as "potentially problematic" and were investigated to find if any bias or systematic problems occurred during data acquisition.

From the overall data set (n = 605), 76% are within < 25% ARD, 14% are between 25% to 50% ARD and only 10% are > 50% ARD (Table 2), which is encouraging and suggests that the new mapping protocol produce near-quantitative measurements that are fit for purpose for most geological contexts. From the overall data quality assessment displayed in Figures 6, 7 and 8, no systematic problems were found regarding matrices, atomic mass or mass fraction level. The atomic masses with the most problems (> 50% ARD) are typically between 185 (Re) and 208 (Pb) which include PGE, Au, W, while masses ranging close to REE are for most < 50% ARD. Both major and minor elements (> 1000 μg g^{-1}) for the most part had < 25% ARD (Figure 8).

The complex interactions in LA-ICP-MS (volatility, condensation, transport, ionisation, etc.) in addition to the level of characterisation and inhomogeneous distribution of the elements in the RM may provide some explanation. Our data suggest that fractionation could differ in the mafic versus felsic nature of the glasses from this experiment, and thus more investigation would be needed to better understand the complexity of multiple matrix-induced fractionation. Extensive testing of the new fast-funnel would also be required to evaluate its impact independently on the presented results. A recent study demonstrated that the fine tuning of laser focus on the surface could be another factor contributing to fractionation (Huang *et al.* 2021), and using a small beam, such as in the present work, is likely to be affected by this parameter and could contribute to the quality of some data. Improving the quality of the data would be profitable, but while homogeneous and well-characterised RMs are mostly limited to glasses, it will remain challenging to achieve. Users should be warned that despite the overall good quality, the data should still be interpreted with caution. This highlights a problem commonly raised about the lack of good quality matrix-matched reference materials for the calibration and quality control of LA-ICP-MS analysis, which is noticeable for sulfide minerals (Günther and Hattendorf 2005, Fernández *et al.* 2007, Danyushevsky *et al.* 2011, Yuan *et al.* 2012, Feng *et al.* 2018, Sio *et al.* 2019, Phyo *et al.* 2020, Steenstra *et al.* 2020). Discussing each occurrence of potential problematic measurement is beyond the scope of this work and more detailed assessment of the quality control of the results for the glass, natural and sulfide reference materials is provided in online supporting information Appendix S1.

New mapping protocol: An example

Figure 9 presents mineral identification based on chemical criteria using the new 3D-TE-DRS (IOLITE) of the mapped area of the sample HN99-46 (Figure 2a). The image is composed of 70,140 pixels of 12 μm and the modal abundance of mineral phases was calculated from the pixels identified by the 3D-TE-DRS (IOLITE) and reported in Table 3. Some features of the sample are not readily visible on the reflected light photomicrograph (Figure 2), such as calcite in the serpentine vein, the fine ilmenite exsolution lamellae in titanomagnetite and the difficult distinction between titanomagnetite and ilmenite. However, the phase identification (Figure 9) highlights their presence and thus can help to support petrographic observation.

Figure 10 presents RGB images produced in IOLITE v4 software of the distribution of major elements, highlighting fine-scale details of a serpentine veinlet (20–50 μm wide) using Si-Al (Figure 10a) and Mg (Figure 10b), as well as some ilmenite exsolution lamellae (5–10 μm wide) in titanomagnetite using Ti (Figure 10b). The ilmenite exsolution lamellae cannot be considered as 100% resolved because the beam used was 12 μm. They were however detected, which is another good example of the fine spatial resolution of the method using the fast-response-funnel (Norris Scientific and Laurin Technic). Figures 10a, b highlight a chemical change of Mg and Si in the micro-veinlets of serpentine when hosted by different minerals. Iron oxide is present in the serpentine vein where titanomagnetite is the host mineral, whereas serpentine mostly fills the vein when apatite is the

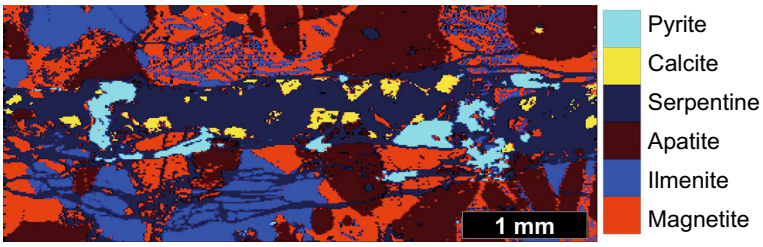

Figure 9. Mineral identification based on chemical criteria, using the new data reduction scheme (IOLITE, 3D-TE-DRS). The map size is 2 mm × 5 mm, pixel resolution is 12 µm, total acquisition time was 46 min.

host mineral. The chemical changes recorded by the new mapping protocol agree with the petrographic observations (Figure 2) and is another demonstration of the resolving power of the new protocol. Figure 10c highlights the relation between S, Mn and Ca. Calcium is present in both apatite and calcite, while Mn is enriched in calcite and present as well in ilmenite and magnetite respectively.

Quality control of major elements in the sample: The IOLITE "Inspector" (Petrus *et al.* 2017, Chew *et al.* 2021) is an elegant tool for the integration of a selected area and was used on the mineral phases to extract major and trace element mass fractions. A comparison of the extracted mineral data from the map with values from EPMA measurement (Nabil 2003, Tollari *et al.* 2008, Méric 2011), SEM analysis (IOS Service Géoscientifiques) and stoichiometry is provided in Table 4. There is consensus for all analytical techniques and stoichiometry for the major element mass fractions in apatite, calcite, ilmenite, and pyrite. The presence of minor components of MgO, FeO and MnO in calcite and MgO in ilmenite is also supported by EPMA/SEM. The Fe form used in magnetite was Fe_3O_4 from the empirical formula $Fe^{3+}{}_2Fe^{2+}O_4$ corresponding to the theoretical presence of FeO (31% *m/m*) and Fe_2O_3 (69% *m/m*) (webmineral.com). The analysis of magnetite and serpentine

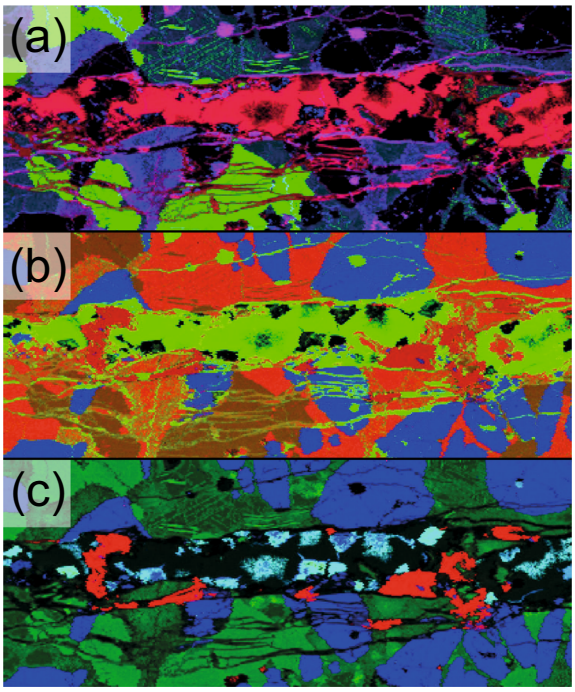

Figure 10. RGB maps of major elements of sample HN99-46. The map is 2 × 5 mm, scale bar is 1 mm. (a) Si (red), Ti (green) and Al (blue); (b) Fe (red), Mg (green) and P (blue); (c) S (red), Mn (green) and Ca (blue).

Table 3.
Modal proportion of mineral abundance in sample HN99-46 based on mineral pixel identification using 3D-TE-DRS (IOLITE)

Phase	*n* pixels	Modal abundance
Pyrite	2,807	4%
Apatite	14,117	20%
Ilmenite	10,744	15%
Serpentine	26,458	38%
Magnetite	14,226	20%
Calcite	1,494	2%
Unidentified	294	0.4%
Total	70,140	100.0%

are good examples to demonstrate that fixing the mass fraction of an internal standard based on stoichiometry could lead to bias of all measured elements. The measured Fe_3O_4 (87%) in the magnetite from sample HN99-46 is lower than the stoichiometry (100% Fe_3O_4) because TiO_2 (8–12%), MgO (0.9–1.2%) and Al_2O_3 (1.8–2.8%) are also present in the natural oxide, as determined in this work and confirmed by EPMA and SEM (Table 4). The chemistry of what we identify as serpentine, does not match any mineral stoichiometry, being somewhere between antigorite ($(Mg,Fe^{2+})_3Si_2O_5(OH)_4$) and corrensite ($(Ca,Na,K)(Mg,Fe,Al)_9(Si,Al)_8O_{20}(OH)_{10}\bullet n(H_2O)$) (Webmineral.com). The measured

Table 4.
Comparison of fully quantitative results for major and minor elements extracted from the HN99-46 map using the IOLITE inspector tool, with results determined by SEM (this study), EPMA (literature) for the same sample and stoichiometry.

Mineral	Source	*n*	F	Cl	CO_2	MgO	Al_2O_3	SiO_2	P_2O_5
Apatite	LA-ICP-ToF-MS	8	nd	nd		0.20			41.73
	1*s*					*0.03*			*0.34*
	SEM (IOS)	2	3.47	0.08		0.21			40.62
	Nabil (2003)	3	3.73	0.09					42.63
	Tollari *et al.* (2008)	10	3.80	0.09		0.12			43.30
	Stoichiometry	-	3.77						42.22
Calcite	LA-ICP-ToF-MS	4			*nd*	0.63			
	1*s*					*0.37*			
	SEM (IOS)	6			46.66	0.42			
	Stoichiometry	-			43.97				
Serpentine	LA-ICP-ToF-MS	5				23.39	1.43	28.96	
	1*s*					*0.14*	*0.05*	*0.17*	
	SEM (IOS)	2				22.17	1.30	34.26	
	Stoichiometry (Antigorite)	-				30.15		39.95	
	Stoichiometry (Corrensite)	-				16.42	12.46	29.38	
Ilmenite	LA-ICP-ToF-MS	4				3.58	0.04	0.02	
	1*s*					*0.28*	*0.01*	*0.02*	
	SEM (IOS)	8				4.46	0.37	0.10	
	Nabil (2003)	3				2.34	0.07		
	Méric (2011)	4				3.53	0.02	0.02	
	Stoichiometry	-							
Magnetite (Type A)	LA-ICP-ToF-MS	3				1.18	1.87	0.35	
	1*s*					*0.14*	*0.18*	*0.28*	
	SEM (IOS)	6				1.13	1.83	0.04	
	Nabil (2003)	3				0.90	2.75		
	Méric (2011)	3				1.15	2.58	0.04	
	Stoichiometry	-							
Mag-A w/ Exsol.	LA-ICP-ToF-MS	4				1.48	1.87	0.11	
	1*s*					*0.26*	*0.16*	*0.04*	
Magnetite (Type B)	LA-ICP-ToF-MS	4				3.70	3.95	4.36	
	1*s*					*0.89*	*1.20*	*1.23*	
	SEM (IOS)	1				3.99	4.30	2.49	
	1*s*					*nd*	*nd*	*nd*	
Pyrite	LA-ICP-ToF-MS	6							
	1*s*								
	Stoichiometry	-							
Biotite	LA-ICP-ToF-MS	1	nd			17.94	11.99	27.89	
	Stoichiometry	-	1.10			23.24	11.76	41.58	

major elements match closely to the SEM data, except that SiO_2 is lower by 20% relative and balanced by 18% relative higher FeO. A matrix effect could explain this difference, such as the presence of water (assumed at 20% by EPMA) that could affect the ablation and ionisation processes relative to the free-H_2O reference material. Using a matrix-matched serpentine as secondary calibrant would be advised in the future. The good overall agreement for the major elements supports the data accuracy of the new mapping protocol (i.e., it is nearly fully quantitative).

Quantification of trace elements: Trace elements cannot be measured by EPMA or SEM or compared with stoichiometry, thus, a series of selected trace element maps are provided and discussed in more details in online supporting information for each main mineral phase (see Figures S5 to S9). In summary, trace element data that were extracted from the map using the inspector tool compared well to LA-ICP-Q-MS values from previous work on this thin section (Tollari *et al.* 2008, Méric 2011, Kieffer *et al.* 2022). The distribution of the measured trace elements are also supported by their partitioning behaviour for the minerals as reported in the literature (Bédard 2001, Dare *et al.* 2012, 2014, Milani *et al.* 2017, Arguin *et al.* 2018, Duran *et al.* 2020). The minimum mass fraction on the scale for each elemental

K_2O	CaO	TiO_2	V_2O_3	MnO	FeO	Fe_3O_4	Fe	S	H_2O	Total
	52.89				0.26					95.1
	0.34				*0.02*					
	55.42				0.32					96.6
	55.16				0.15					97.9
	53.28				0.15					96.9
	55.60									97.8
	52.85			1.40	0.39					55.3
	0.47			*0.34*	*0.12*					
	50.90			1.25	0.83					53.4
	56.03									56.0
0.06	0.22			0.132	25.06				nd	79.3
0.01	*0.03*			*0.002*	*0.32*					
				0.125	21.99				nd	79.8
					17.92				11.98	100.0
0.77	2.74				17.56				20.55	99.9
		52.18	0.024	0.75	42.98					99.6
		1.48	*0.002*	*0.01*	*1.90*					
		52.11	0.48	0.79	42.30					100.6
		50.90		0.77	44.93					99.0
		52.18	0.13	0.72	41.66					98.3
		52.65			47.35					100.0
		9.59	0.34	0.52		85.69				99.5
		0.44	*0.02*	*0.16*		*0.49*				
		9.35	0.53	0.41		86.70				100.0
		11.66	0.63	0.40		82.64				99.0
		9.05	0.59	0.31		84.53				98.2
						100.00				100.0
		12.00	0.35	0.40		84.44				100.6
		3.08	*0.05*	*0.05*		*2.69*				
0.07		8.25	0.29	0.56		76.64				97.8
0.04		*0.73*	*0.04*	*0.06*		*2.54*				
0.09		9.52	0.49	0.43		78.69				100.0
nd		*nd*	*nd*	*nd*		*nd*				
							49.07	50.48		99.6
							0.58	*0.15*		
							46.55	53.45		100.0
9.63					8.39				nd	75.8
10.86					8.29				3.64	99.4

map was fixed to their respective LLoD, thus removing any pixel < LLoD.

Ablation yield and total effective yield (TEY): As previously mentioned, internal standardisation or normalisation is necessary to correct for differences in ablation yield to achieve fully-quantitative measurement (Jackson *et al.* 1992, Jochum and Stoll 2008, Liu *et al.* 2008). The overall signal response in certain phases such as iron oxide is lower compared with more easily ablated phases, such as sulfide and hydrated silicate (see Table 5 and discussions below). Semi-quantitative or qualitative approaches in LA-ICP-MS mapping are often based on the raw signal and reported in terms of raw counts per second (McCarron *et al.* 2014, Ubide *et al.* 2015, Cook *et al.* 2016, Zhu *et al.* 2016, Gourcerol *et al.* 2018). Although it can be very useful, this approach can still represent a risk that can potentially lead to erroneous results and interpretation, not only for the mass fraction (semi-quantitative) of the elements in each phase, but also in the perception of their spatial distribution. It is thus essential to underline the importance of tracking and apply corrections regarding the ablation yield when no fixed internal standard element can be used. This work supports

Table 5.
Total effective yield table (TEY) of different natural minerals relative to Magnetite Type-A (from sample HN99-46)

Mineral (sample HN99-46)	Relative yield
Magnetite Type-A	1.00
Apatite	1.05
Magnetite Type-B	1.11
Magnetite Type-A w/Exsol	1.12
Ilmenite	1.18
Biotite	1.42
Calcite	1.67
Serpentine	2.29
Pyrite	4.54

the useful normalisation approach and highlights the risk of potential error associated with mapping using semi-quantitative analysis or raw counts to study elemental distribution in the analysed samples.

The laser ablation yield is described as the amount of material ablated (Jeffries *et al.* 1995) and can be affected by the depth of ablation, the laser conditions (wavelength, energy, beam size) in addition to the physical and chemical properties of the ablated material (Koch *et al.* 2008, Van Malderen *et al.* 2016). The rate of ablated material can significantly differ amongst different minerals and will have an effect on the sensitivity, but a multitude of complex interacting processes, such as transport and ionisation in the plasma, are also involved in the detection of atomic components (Van Malderen *et al.* 2016). Consequently, the term "ablation yield" is more appropriate to designate the amount of ablated material, while we propose to use the "total effective yield" (TEY) to include all accumulated causes that influence the variation of sensitivity between the ablated phases. To our knowledge, no detailed information is available about the relative TEY between phases, although this information can be easily extracted from a quantitative analysis (map and reference materials). Using the IOLITE calculator tool (Petrus *et al.* 2017), the TEY of mineral phases using six major elements (Fe, Mg, Si, Al, Ca and S) were obtained by dividing the mass fraction (μg g^{-1}) with their net count per seconds (ToF ions/extraction). The six major elements provided similar distributions of the TEY, with the example of Fe plotted in Figure 11, illustrating that sulfide clearly has a higher TEY than the other phases. Results extracted from the ToF map using the inspector tool, along with the six minerals from the sample are provided in Table 5. The unaltered titanomagnetite (Type-A) in the mapped sample has the lowest TEY and was thus used as the reference for relative comparison with other materials (Table 5). The TEY of other oxides (chromite, ilmenite and rutile) and apatite are comparable (< 1.18), while pyrite is the mineral with the highest TEY (4.54) relative to titanomagnetite Type-A. An extended relative TEY table comprising a total of thirty-one samples, analysed in the same condition as of the present work, and including reference materials and other natural minerals is available in Table S5. As underlined by Cook *et al.* (2016), mass fraction cannot be inferred across different phases from the raw signal. An example of such an effect on the Fe and Ti distribution is provided in Figure 12, where the normalised mass fraction maps determined in this study are compared with the raw signal maps. The raw signal map of Fe (Figure 12a) suggests at first that Fe in the pyrite is much higher than any other phases, whereas Fe is actually higher in the magnetite phase, as shown on the quantitative map (Figure 12b). On the other hand, the raw signal map of titanium (Figure 12c) is almost similar to the quantitative Ti map (Figure 12d) because Ti is mainly present in ilmenite and magnetite, and these two phases have comparable TEYs (Table 5).

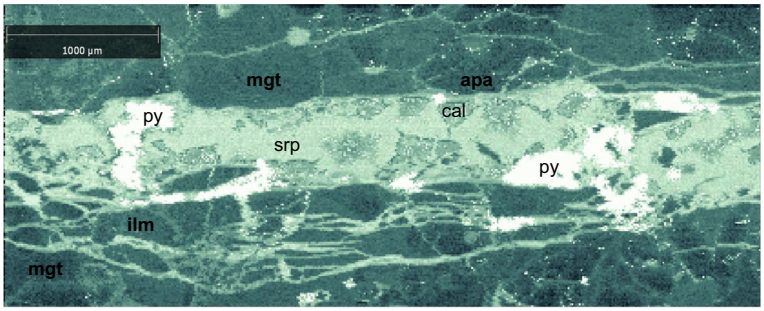

Figure 11. Distribution of the calculated "total effective yield" (TEY) for Fe in the sample HN99-46; (srp) serpentine, (apa) apatite, (mag) magnetite, (ilm) ilmenite, (py) pyrite, (cal) calcite.

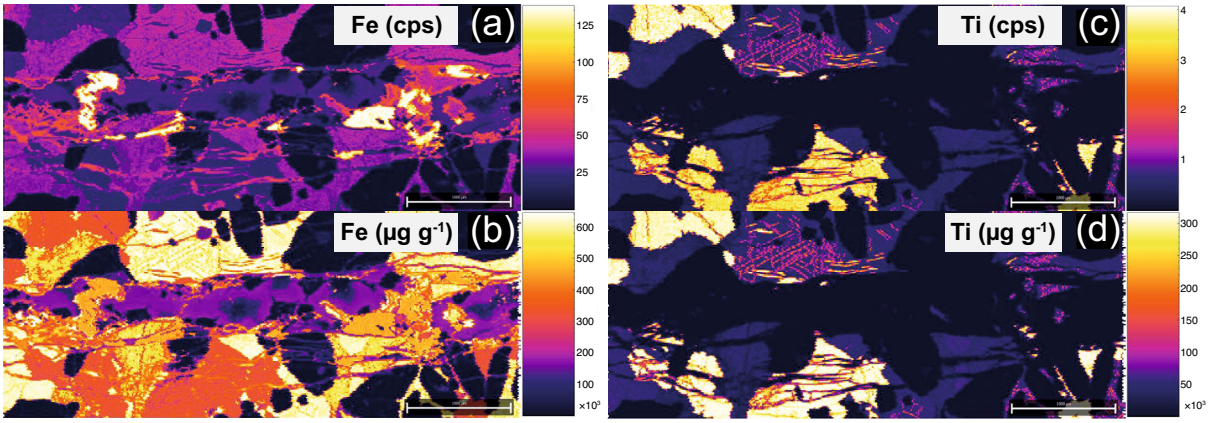

Figure 12. Comparison of raw signal to normalised mass fraction in sample HN99-46. (a) Fe non-corrected raw count detection, (b) Fe (µg g^{-1}) normalised quantitative, (c) Ti (non-corrected raw count detection) and (d) normalised quantitative Ti (µg g^{-1}). The Fe distribution differs significantly while Ti had quite similar distribution.

Conclusions

A new LA-ICP-MS protocol for the simultaneous determination of trace and major elements in multiple minerals combining a 193 nm laser equipped with a fast-funnel device and coupled to a time-of-flight mass spectrometer is presented. The technique combined multiple reference materials of varied matrices (sulfide, mafic-glasses, felsic-glasses, natural apatite) to produce blocks of calibration. The data were quantified using a recently developed data reduction scheme in IOLITE v4 (3D-TE-DRS). The protocol thus provides an extended coverage of the elements and points toward best practice in LA-ICP-MS by using (multiple) matrix-matched calibration materials. Mineral recognition is possible using the new IOLITE 3D-TE-DRS, and appropriate conversion of oxide forms is applied and correction for undetected components such as CO_2, F, Cl, H_2O is possible to achieve quantitative results by personalised normalisation for contrasting minerals such as sulfides, silicates and carbonates. The normalisation to 100% oxide approach avoids having to use external determination of major elements, by for example electron microprobe analysis, to use as internal standards. In addition, we introduce the concept of "total effective yield" (TEY) and show that there can be significant difference between some minerals, which emphasises the importance of the normalisation approach to achieve quantitative measurement. The technique has the advantage of producing chemical images at a rate of 30 pixels s^{-1}, which is about ten times faster compared with methods for quadrupole-MS. The analysis of multiple quality control reference materials and a comparison of the analysed minerals with other external sources (LA-ICP-MS, SEM, EPMA) demonstrated that the quality of the data fit the purpose. However, like any methods under development, there is room for improvement. The proximity of limits of detection, confidence on the working mass fractions of the reference material used, possible fast-funnel induced fractionation, or problems with the tuning of the ICP-ToF-MS itself are to be improved but are beyond the scope of this work. Consequently, users must be aware that uncertainties can affect the measurement results. In summary, the protocol offers efficiency and high analytical speed for fine resolution chemical mapping of trace and major elements over much larger areas than previously available.

Acknowledgements

The ToF-ICP-MS instrument was bought and operated using the Canada Foundation of Innovation (CFI) Fund (#36357) and Infrastructure Operating Fund of S.-J. Barnes at LabMaTer, UQAC. This study was financed by LabMaTer (UQAC), the Canada Research Chair in Geochemistry Applied to Ore Deposits (CRC-2017-0286) (S. Dare, LabMaTer) and La Fondation de l'UQAC (Université du Québec à Chicoutimi) to S. Dare and L.P. Bédard for the Ph.D. project of D. Savard. Joe Petrus and Bence Paul (IOLITE), Ashley Norris (Norris Scientific), Mike Shelley (Laurin Technic), and Martin Tanner and Martin Rittner (TOFWERK) are warmly thanked for their precious support, advice and development with the equipment and software. We are grateful to Audrey Lavoie (Technician at LabMaTer) for her support in the laboratory and Jonathan Tremblay at IOS Services Géoscientifiques for the SEM analysis. We also want to thank the editor and anonymous reviewers for their critical and very helpful comments and

suggestions. There are no conflicts of interests of author and co-author.

Data availability statement

Data sharing is not applicable to this article as no new data were created or analyzed in this study.

References

Andronikov A.V., Andronikova I.E. and Sidorinova T. (2021)
Trace-element geochemistry of sulfides in upper mantle lherzolite xenoliths from east Antarctica. Minerals, 11, 1–32.

Arguin J.-P., Pagé P., Barnes S.-J., Yu S.-Y. and Song X.-Y. (2016)
The effect of chromite crystallization on the distribution of osmium, iridium, ruthenium and rhodium in picritic magmas: An example from the Emeishan large igneous province, southwestern China. Journal of Petrology, 57, 1019–1048.

Arguin J.-P., Pagé P., Barnes S.-J., Girard R. and Duran C. (2018)
An integrated model for ilmenite, Al-spinel, and corundum exsolutions in titanomagnetite from oxide-rich layers of the Lac Doré Complex (Québec, Canada). Minerals, 8, 476.

Aulbach S., Giuliani A., Fiorentini M.L., Baumgartner R.J., Savard D., Kamenetsky V.S., Caruso S., Danyushevky L.V., Powell W. and Griffin W.L. (2021)
Siderophile and chalcophile elements in spinels, sulphides and native Ni in strongly metasomatised xenoliths from the Bultfontein kimberlite (South Africa). Lithos, 380, 105880.

Batanova V.G., Thompson J.M., Danyushevsky L.V., Portnyagin M.V., Garbe-Schönberg D., Hauri, E., Kimura J.I., Chang Q., Senda R., Goemann K., Chauvel C., Campillo S., Ionov D.A. and Sobolev A.V. (2019)
New olivine reference material for *in situ* microanalysis. Geostandards and Geoanalytical Research, 43, 453–473.

Bédard J.H. (2001)
Parental magmas of the Nain Plutonic Suite anorthosites and mafic cumulates: A trace element modelling approach. Contributions to Mineralogy and Petrology, 141, 747–771.

Bleiner D., Hametner K. and Günther D. (2000)
Optimization of a laser ablation-inductively coupled plasma "time of flight" mass spectrometry system for short transient signal acquisition. Fresenius' Journal of Analytical Chemistry, 368, 37–44.

Borovinskaya O. (2014)
A new inductively coupled plasma time-of-flight mass spectrometer: Fundamentals and applications. PhD Thesis, ETH Zürich, 160pp.

Burger M., Schwarz G., Gundlach-Graham A., Käser D., Hattendorf B. and Günther D. (2017)
Capabilities of laser ablation inductively coupled plasma time-of-flight mass spectrometry. Journal of Analytical Atomic Spectrometry, 32, 1946–1959.

Burger M., Hendriks L., Kaeslin J., Gundlach-Graham A., Hattendorf B. and Günther D. (2019)
Characterization of inductively coupled plasma time-of-flight mass spectrometry in combination with collision/reaction cell technology – Insights from highly time-resolved measurements. Journal of Analytical Atomic Spectrometry, 34, 135–146.

Bussweiler Y., Borovinskaya O. and Tanner M. (2017)
Laser ablation and inductively coupled plasma-time-of-flight mass spectrometry – A powerful combination for high-speed multielemental imaging on the micrometer scale. Spectroscopy, 32, 14–20.

Bussweiler Y., Gervasoni F., Rittner M., Berndt J. and Klemme S. (2020)
Trace element mapping of high-pressure, high-temperature experimental samples with laser ablation ICP time-of-flight mass spectrometry – Illuminating melt-rock reactions in the lithospheric mantle. Lithos, 352, 105282pp.

Chew D., Drost K., Marsh J.H. and Petrus J.A. (2021)
LA-ICP-MS imaging in the geosciences and its applications to geochronology. Chemical Geology, 559, 119917.

Chew D.M., Babechuk M.G., Cogné N., Mark C., O'Sullivan G.J., Henrichs I.A., Doepke D. and McKenna C.A. (2016)
(LA,Q)-ICP-MS trace-element analyses of Durango and McClure Mountain apatite and implications for making natural LA-ICP-MS mineral standards. Chemical Geology, 435, 35–48.

Conde J.C., Lusquiños F., González P., Serra J., León B., Dima A., Cultrera L., Guido D., Zocco A. and Perrone A. (2004)
Finite element analysis of the initial stages of the laser ablation process. Thin Solid Films, 453–454, 323–327.

Cook N., Ciobanu C., George L., Zhu Z.-Y., Wade B. and Ehrig K. (2016)
Trace element analysis of minerals in magmatic-hydrothermal ores by laser ablation inductively-coupled plasma-mass spectrometry: Approaches and opportunities. Minerals, 6, 111.

Danyushevsky L., Robinson P., Gilbert S., Norman M., Large R., McGoldrick P. and Shelley M. (2011)
Routine quantitative multi-element analysis of sulphide minerals by laser ablation ICP-MS: Standard development and consideration of matrix effects. Geochemistry: Exploration, Environment, Analysis, 11, 51–60.

Dare S.A., Barnes S.-J. and Beaudoin G. (2012)
Variation in trace element content of magnetite crystallized from a fractionating sulfide liquid, Sudbury, Canada: Implications for provenance discrimination. Geochimica et Cosmochimica Acta, 88, 27–50.

Dare S.A., Barnes S.-J., Beaudoin G., Méric J., Boutroy E. and Potvin-Doucet C. (2014)
Trace elements in magnetite as petrogenetic indicators. Mineralium Deposita, 49, 785–796.

references

Douglas D.N., Managh A.J., Reid H.J. and Sharp B.L. (2015)
High-speed, integrated ablation cell and dual concentric injector plasma torch for laser ablation-inductively coupled plasma-mass spectrometry. Analytical Chemistry, 87, 11285–11294.

Duparc Q., Dare S.A.S., Cousineau P.A. and Goutier J. (2016)
Magnetite chemistry as a provenance indicator in Archean metamorphosed sedimentary rocks. Journal of Sedimentary Research, 86, 542–563.

Dupuis C. and Beaudoin G. (2011)
Discriminant diagrams for iron oxide trace element fingerprinting of mineral deposit types. Mineralium Deposita, 46, 319–335.

Duran C.J., Barnes S.-J., Mansur E.T., Dare S.A.S., Bédard L.P. and Sluzhenikin S.F. (2020)
Magnetite chemistry by LA-ICP-MS records sulfide fractional crystallization in massive nickel-copper-platinum-group element ores from the Norilsk-Talnakh mining district (Siberia, Russia): Implications for trace element partitioning into magnetite. Economic Geology, 115, 1245–1266.

Duran C.J., Dubé-Loubert H., Pagé P., Barnes S.-J., Roy M., Savard D., Cave B.J., Arguin J.-P. and Mansur E.T. (2019)
Applications of trace element chemistry of pyrite and chalcopyrite in glacial sediments to mineral exploration targeting: Example from the Churchill Province, northern Quebec, Canada. Journal of Geochemical Exploration, 196, 105–130.

Eggins S.M. and Shelley J.M.G. (2002)
Compositional heterogeneity in NIST SRM 610–617 glasses. Geostandards Newsletter: The Journal of Geostandards and Geoanalysis, 26, 269–286.

Feng Y., Zhang W., Hu Z., Liu Y., Chen K., Fu J., Xie J. and Shi Q. (2018)
Development of sulfide reference materials for *in situ* platinum-group elements and S–Pb isotope analyses by LA-(MC)-ICP-MS. Journal of Analytical Atomic Spectrometry, 33, 2172–2183.

Fernández B., Claverie F., Pécheyran C., Donard O.F.X. and Claverie F. (2007)
Direct analysis of solid samples by fs-LA-ICP-MS. TrAC Trends in Analytical Chemistry, 26, 951–966.

Fricker M.B., Kutscher D., Aeschlimann B., Frommer J., Dietiker R., Bettmer J. and Günther D. (2011)
High spatial resolution trace element analysis by LA-ICP-MS using a novel ablation cell for multiple or large samples. International Journal of Mass Spectrometry, 307, 39–45.

Gagnon J.E., Fryer B.J., Samson I.M. and Williams-Jones A.E. (2008)
Quantitative analysis of silicate certified reference materials by LA-ICP-MS with and without an internal standard. Journal of Analytical Atomic Spectrometry, 23, 1529–1537.

Garbe-Schönberg D. and Müller S. (2014)
Nano-particulate pressed powder tablets for LA-ICP-MS. Journal of Analytical Atomic Spectrometry, 29, 990–1000.

Gilbert S., Danyushevsky L., Robinson P., Wohlgemuth-Ueberwasser C., Pearson N., Savard D., Norman M. and Hanley J. (2013)
A comparative study of five reference materials and the Lombard meteorite for the determination of the platinum-group elements and gold by LA-ICP-MS. Geostandards and Geoanalytical Research, 37, 51–64.

Gourcerol B., Kontak D.J., Thurston P.C. and Petrus J.A. (2018)
Application of LA-ICP-MS sulfide analysis and methodology for deciphering elemental paragenesis and associations in addition to multi-stage processes in metamorphic gold settings. The Canadian Mineralogist, 56, 39–64.

Guilmette C., Smit M.A., van Hinsbergen D.J., Gürer D., Corfu F., Charette B., Maffione M., Rabeau O. and Savard D. (2018)
Forced subduction initiation recorded in the sole and crust of the Semail Ophiolite of Oman. Nature Geoscience, 11, 688.

Gundlach-Graham A. and Günther D. (2016)
Toward faster and higher resolution LA-ICP-MS imaging: On the co-evolution of LA cell design and ICP-MS instrumentation. Analytical and Bioanalytical Chemistry, 408, 2687–2695.

Gundlach-Graham A., Garofalo P.S., Schwarz G., Redi D. and Günther D. (2018)
High-resolution, quantitative element imaging of an upper crust, low-angle cataclasite (Zuccale Fault, northern Apennines) by laser ablation ICP time-of-flight mass spectrometry. Geostandards and Geoanalytical Research, 42, 559–574.

Günther D. and Hattendorf B. (2005)
Solid sample analysis using laser ablation inductively coupled plasma-mass spectrometry. TrAC Trends in Analytical Chemistry, 24, 255–265.

Hattendorf B., Hartfelder U. and Günther D. (2019)
Skip the beat: Minimizing aliasing error in LA-ICP-MS measurements. Analytical and Bioanalytical Chemistry, 411, 591–602.

Hendriks L., Gundlach-Graham A., Hattendorf B. and Günther D. (2017)
Characterization of a new ICP-ToFMS instrument with continuous and discrete introduction of solutions. Journal of Analytical Atomic Spectrometry, 32, 548–561.

Huang H.-Q., Guillong M., Hu Y. and Spandler C. (2021)
Fine tuning laser focus for improved reproducibility of U–Pb isotope analysis by LA-ICP-MS. Journal of Analytical Atomic Spectrometry, 36, 836–844.

references

Jackson S.E., Longerich H.P., Dunning G.R. and Fryer B.J. (1992)
The application of laser ablation microprobe-inductively coupled plasma-mass spectrometry (LAM-ICP-MS) to *in situ* trace-element determinations in minerals. The Canadian Mineralogist, 30, 1049–1064.

Jeffries T., Perkins W. and Pearce N. (1995)
Measurements of trace elements in basalts and their phenocrysts by laser probe microanalysis inductively coupled plasma-mass spectrometry (LPMA-ICP-MS). Chemical Geology, 121, 131–144.

Jochum K.P. and Stoll B. (2008)
Reference materials for elemental and isotopic analyses by LA-(MC)-ICP-MS: Successes and outstanding needs. **In:** Sylvester P. (ed.), Laser ablation ICP-MS in the Earth sciences: Current practices and outstanding issues. Mineralogical Association of Canada, 40, 147–168.

Jochum K.P., Garbe-Schönberg D., Veter M., Stoll B., Weis U., Weber M., Lugli F., Jentzen A., Schiebel R., Wassenburg J.A., Jacob D.E. and Haug G.H. (2019)
Nano-powdered calcium carbonate reference materials: Significant progress for microanalysis? Geostandards and Geoanalytical Research, 43, 595–609.

Kelly C.J., Schneider D.A., Jackson S.E., Kalbfleisch T. and McFarlane C.R. (2017)
Insights into low- to moderate-temperature recrystallization of zircon: Unpolished crystal depth profile techniques and geochemical mapping. Chemical Geology, 449, 82–98.

Kieffer M.A., Dare S.A.S. and Namur O. (2022)
The use of trace elements in apatite to trace differentiation of a ferrobasaltic melt in the Sept-Iles Intrusive Suite, Quebec, Canada: Implications for provenance discrimination. Geochimica et Cosmochimica Acta, 342, 169–197.

Koch J., Wälle M., Dietiker R. and Günther D. (2008)
Analysis of laser-produced aerosols by inductively coupled plasma-mass spectrometry: Transport phenomena and elemental fractionation. Analytical Chemistry, 80, 915–921.

Lawley C.J.M., Petts D.C., Jackson S.E., Zagorevski A., Pearson D.G., Kjarsgaard B.A., Savard D. and Tschirhart V. (2020)
Precious metal mobility during serpentinization and breakdown of base metal sulphide. Lithos, 354, 105278pp.

Lazartigues A.V., Sirois P. and Savard D. (2014)
LA-ICP-MS analysis of small samples: Carbonate reference materials and larval fish otoliths. Geostandards and Geoanalytical Research, 38, 225–240.

Lear J., Hare D., Adlard P., Finkelstein D. and Doble P. (2012)
Improving acquisition times of elemental bio-imaging for quadrupole-based LA-ICP-MS. Journal of Analytical Atomic Spectrometry, 27, 159–164.

Liu Y., Hu Z., Gao S., Günther D., Xu J., Gao C. and Chen H. (2008)
In situ analysis of major and trace elements of anhydrous minerals by LA-ICP-MS without applying an internal standard. Chemical Geology, 257, 34–43.

Longerich H.P., Jackson S.E. and Günther D. (1996)
Inter-laboratory note. Laser ablation inductively coupled plasma-mass spectrometric transient signal data acquisition and analyte concentration calculation. Journal of Analytical Atomic Spectrometry, 11, 899–904.

Lyons J.I. (1988)
Volcanogenic iron oxide deposits, Cerro de Mercado and vicinity, Durango. Economic Geology, 83, 1886–1906.

Macholdt D.S., Jochum K.P., Stoll B., Weis U. and Andreae M.O. (2014)
A new technique to determine element amounts down to femtograms in dust using femtosecond laser ablation-inductively coupled plasma-mass spectrometry. Chemical Geology, 383, 123–131.

Mao M., Simandl G.J., Spence J., Marshall D. and Neetz M. (2015)
Fluorite trace-element chemistry and its potential as an indicator mineral: Evaluation of LA-ICP-MS method. **In:** Simandl G.J. and Neetz M. (eds), Symposium on strategic and critical materials: Proceedings. British Columbia Geological Survey Paper, 3, 251–264.

McCarron T., Gaidies F., McFarlane C.R.M., Easton R.M. and Jones P. (2014)
Coupling thermodynamic modeling and high-resolution *in situ* LA-ICP-MS monazite geochronology: Evidence for Barrovian metamorphism late in the Grenvillian history of southeastern Ontario. Mineralogy and Petrology, 108, 741–758.

Méric J. (2011)
Caractérisation géochimiques des magnétites de la zone critique de l'intrusion magmatique de Sept-Iles (Québec, Canada) et intégration a une base de données utilisant la signature géochimique des oxydes de fer comme outil d'exploration. Rapport de Stage de fin d'étude du Master, Université du Québec à Chicoutimi-Université Montpellier 2, 48pp.

Milani L., Bolhar R., Cawthorn R.G. and Frei D. (2017)
In situ LA-ICP-MS and EPMA trace element characterization of Fe–Ti oxides from the phoscorite–carbonatite association at Phalaborwa, South Africa. Mineralium Deposita, 52, 747–768.

Moradi A.B., Swoboda S., Robinson B., Prohaska T., Kaestner A., Oswald S.E., Wenzel W.W. and Schulin R. (2010)
Mapping of nickel in root cross-sections of the hyperaccumulator plant *Berkheya coddii* using laser ablation ICP-MS. Environmental and Experimental Botany, 69, 24–31.

Müller W., Shelley M., Miller P. and Broude S. (2009)
Initial performance metrics of a new custom-designed ArF excimer LA-ICP-MS system coupled to a two-volume laser-ablation cell. Journal of Analytical Atomic Spectrometry, 24, 209–214.

Myers D., Li G., Yang P. and Hieftje G. (1994)
An inductively coupled plasma-time-of-flight mass spectrometer for elemental analysis. Part I: Optimization and characteristics. Journal of the American Society for Mass Spectrometry, 5, 1008–1016.

references

Nabil H. (2003)
Genèse des dépôts de Fe-Ti-P associés aux intrusions litées (exemples: l'intrusion mafique de Sept-Iles, au Québec; complexe de Duluth aux États-Unis). Thèse de Doctorat, Université du Québec à Chicoutimi, 537pp.

Nadoll P. and Koenig A.E. (2011)
LA-ICP-MS of magnetite: Methods and reference materials. Journal of Analytical Atomic Spectrometry, 26, 1872–1877.

Neff C., Keresztes Schmidt P., Garofalo P.S., Schwarz G. and Günther D. (2020)
Capabilities of automated LA-ICP-TOFMS imaging of geological samples. Journal of Analytical Atomic Spectrometry, 35, 2255–2266.

Norris C.A., Danyushevsky L., Olin P. and West N.R. (2021)
Elimination of aliasing in LA-ICP-MS by alignment of laser and mass spectrometer. Journal of Analytical Atomic Spectrometry, 36, 733–739.

Pan Y., Hu L. and Zhao T. (2019)
Applications of chemical imaging techniques in paleontology. National Science Review, 6, 1040–1053.

Paton C., Hellstrom J., Paul B., Woodhead J. and Hergt J. (2011)
Iolite: Freeware for the visualisation and processing of mass spectrometric data. Journal of Analytical Atomic Spectrometry, 26, 2508–2518.

Paul B., Woodhead J.D., Paton C., Hergt J.M., Hellstrom J. and Norris C.A. (2014)
Towards a method for quantitative LA-ICP-MS imaging of multi-phase assemblages: Mineral identification and analysis correction procedures. Geostandards and Geoanalytical Research, 38, 253–263.

Petrus J., Chew D., Leybourne M. and Kamber B. (2017)
A new approach to laser ablation-inductively coupled plasma-mass spectrometry (LA-ICP-MS) using the flexible map interrogation tool 'Monocle'. Chemical Geology, 463, 76–93.

Phyo M.M., Wang H.A.O., Guillong M., Berger A., Franz L., Balmer W.A. and Krzemnicki M.S. (2020)
U–Pb dating of zircon and zirconolite inclusions in marble-hosted gem-quality ruby and spinel from Mogok, Myanmar. Minerals, 10, 195.

Pisonero J., Fliegel D. and Günther D. (2006)
High efficiency aerosol dispersion cell for laser ablation-ICP-MS. Journal of Analytical Atomic Spectrometry, 21, 922–931.

Raimondo T., Payne J., Wade B., Lanari P., Clark C. and Hand M. (2017)
Trace element mapping by LA-ICP-MS: Assessing geochemical mobility in garnet. Contributions to Mineralogy and Petrology, 172, 1–22.

Rubatto D., Burger M., Lanari P., Hattendorf B., Schwarz G., Neff C., Keresztes Schmidt P., Hermann J., Vho A. and Günther D. (2020)
Identification of growth mechanisms in metamorphic garnet by high-resolution trace element mapping with LA-ICP-ToF-MS. Contributions to Mineralogy and Petrology, 175, 61.

Sanborn M. and Telmer K. (2003)
The spatial resolution of LA-ICP-MS line scans across heterogeneous materials such as fish otoliths and zoned minerals. Journal of Analytical Atomic Spectrometry, 18, 1231–1237.

Savard D., Barnes S.-J., Dare S.A. and Beaudoin G. (2012)
Improved calibration technique for magnetite analysis by LA-ICP-MS. Mineralogical Magazine, 76, 2329.

Savard D., Bouchard-Boivin B., Barnes S. and Garbe-Schönberg D. (2018)
UQAC-FeS: A new series of base metal sulfide quality control reference material for LA-ICP-MS analysis. Proceedings of the 10th International Conference on the Analysis of Geological and Environmental Materials, Sydney, Australia, 8–13.

Savard D., Dare S.A.S., Bédard L.P., Barnes S.-J. and Petrus J. (2021)
Development of an extended matrix-matched calibration protocol for fast, high-resolution, quantitative chemical mapping of major and trace elements of polymineralic samples by laser-ablation coupled to time-of-flight-mass-spectrometry (LA-ICP-TOF-MS). Goldschmidt 2021 Virtual Conference.

Selih V.S. and van Elteren J.T. (2011)
Quantitative multi-element mapping of ancient glass using a simple and robust LA-ICP-MS rastering procedure in combination with image analysis. Analytical and Bioanalytical Chemistry, 401, 745–755.

Sio C.K., Parsons-Davis T., Lee E., Wimpenny J., Pascall A.J., Kuntz J.D., Goodell J.J., Roberts K.E., Bandong B.B. and Bennett N.R. (2019)
Additive manufacturing of platinum-group element (PGE) standard reference materials with a silica matrix. Rapid Communications in Mass Spectrometry, 34, e8627.

Smythe D., Schulze D. and Brenan J. (2008)
Rutile as a kimberlite indicator mineral: Minor and trace element geochemistry. International Kimberlite Conference: Extended Abstracts. Vol. 9.

Steenstra E., Berndt J., Klemme S., Van Westrenen W., Bullock E. and Shahar A. (2020)
Addressing matrix effects for 193 nm excimer LA-ICP-MS analyses of Fe-rich sulfides and a new predictive model. Journal of Analytical Atomic Spectrometry, 35, 498–509.

references

Sugiono D., LaFlamme C., Thébaud N., Martin L., Savard D. and Fiorentini M. (2022)
Fault-induced gold saturation of a single auriferous fluid is a key process for orogenic gold deposit formation. Economic Geology, 117, 1405–1414.

Sylvester P.J. and Jackson S.E. (2016)
A brief history of laser ablation-inductively coupled plasma-mass spectrometry (LA-ICP-MS). Elements, 12, 307–310.

Tanner M. and Günther D. (2008)
A new ICP-TOFMS. Measurement and readout of mass spectra with 30 µs time resolution, applied to in-torch LA-ICP-MS. Analytical and Bioanalytical Chemistry, 391, 1211–1220.

Theiner S., Schoeberl A., Schweikert A., Keppler B.K. and Koellensperger G. (2021)
Mass spectrometry techniques for imaging and detection of metallodrugs. Current Opinion in Chemistry and Biology, 61, 123–134.

Thompson J.A., Thompson J.M., Goemann K., Lounejeva E., Cooke D.R. and Danyushevsky L. (2021a)
Use of non-matrix matched reference materials for the accurate analysis of calcium carbonate by LA-ICP-MS. Geostandards and Geoanalytical Research, 46, 97–115.

Thompson J.M., Danyushevsky L.V., Borovinskaya O. and Tanner M. (2020)
Time-of-flight ICP-MS laser ablation zircon geochronology: Assessment and comparison against quadrupole ICP-MS. Journal of Analytical Atomic Spectrometry, 35, 2282–2297.

Thompson J.M., Goemann K., Belousov I., Jenkins K., Kobussen A., Powell W. and Danyushevsky L. (2021b)
Assessment of the mineral ilmenite for U–Pb dating by LA-ICP-MS. Journal of Analytical Atomic Spectrometry, 36, 1244–1260.

Tollari N., Barnes S.-J., Cox R.A. and Nabil H. (2008)
Trace element concentrations in apatites from the Sept-Îles Intrusive Suite, Canada – Implications for the genesis of nelsonites. Chemical Geology, 252, 180–190.

Ubide T., McKenna C.A., Chew D.M. and Kamber B.S. (2015)
High-resolution LA-ICP-MS trace element mapping of igneous minerals: In search of magma histories. Chemical Geology, 409, 157–168.

Ubide T., Caulfield J., Brandt C., Bussweiler Y., Mollo S., Di Stefano F., Nazzari M. and Scarlato P. (2019)
Deep magma storage revealed by multi-method elemental mapping of clinopyroxene megacrysts at Stromboli volcano. Frontiers in Earth Science, 7, 239pp.

Van Acker T., Van Malderen S.J., Van Helden T., Stremtan C., Šala M., van Elteren J.T. and Vanhaecke F. (2021)
Analytical figures of merit of a low-dispersion aerosol transport system for high-throughput LA-ICP-MS analysis. Journal of Analytical Atomic Spectrometry, 36, 1201–1209.

van Elteren J.T., Sala M. and Metarapi D. (2021)
Comparison of single pulse, multiple dosage, and 2D oversampling / deconvolution LA-ICP-MS strategies for mapping of (ultra)low-concentration samples. Talanta, 235, 122785.

Van Malderen S.J., van Elteren J.T. and Vanhaecke F. (2015)
Development of a fast laser ablation-inductively coupled plasma-mass spectrometry cell for sub-µm scanning of layered materials. Journal of Analytical Atomic Spectrometry, 30, 119–125.

Van Malderen S.J., Managh A.J., Sharp B.L. and Vanhaecke F. (2016)
Recent developments in the design of rapid response cells for laser ablation-inductively coupled plasma-mass spectrometry and their impact on bioimaging applications. Journal of Analytical Atomic Spectrometry, 31, 423–439.

Wang H.A., Grolimund D., Giesen C., Borca C.N., Shaw-Stewart J.R., Bodenmiller B. and Günther D. (2013)
Fast chemical imaging at high spatial resolution by laser ablation inductively coupled plasma-mass spectrometry. Analytical Chemistry, 85, 10107–10116.

Wilson S., Ridley W. and Koenig A. (2002)
Development of sulfide calibration standards for the laser ablation inductively-coupled plasma-mass spectrometry technique. Journal of Analytical Atomic Spectrometry, 17, 406–409.

Yuan J.-H., Zhan X.-C., Fan C.-Z., Zhao L.-H., Sun D.-Y., Jia Z.-R., Hu M.-Y. and Kuai L.-J. (2012)
Quantitative analysis of sulfide minerals by laser ablation-inductively coupled plasma-mass spectrometry using glass reference materials with matrix normalization plus sulfur internal standardization calibration. Chinese Journal of Analytical Chemistry, 40, 201–207.

Zhou L., McKenna C.A., Long D.G.F. and Kamber B.S. (2017)
LA-ICP-MS elemental mapping of pyrite: An application to the Palaeoproterozoic atmosphere. Precambrian Research, 297, 33–55.

Zhu Z.-Y., Cook N.J., Yang T., Ciobanu C.L., Zhao K.-D. and Jiang S.-Y. (2016)
Mapping of sulfur isotopes and trace elements in sulfides by LA-(MC)-ICP-MS: Potential analytical problems, improvements and implications. Minerals, 6, 110.

Supporting information

The following supporting information may be found in the online version of this article:

Figure S1. Sampling modes: (a) pulse-by-pulse and vertical drilling modes using a round beam; (b, c) beams of equal horizontal width and vertical length lead to over-sampling areas; (d) a rectangular beam (height: length of 2:1).

Figure S2. Screen capture from IOLITE v4 3D-TE-DRS showing examples of calibration using multiple reference

materials (NIST SRM 610, GSD-1G, GSE-1G, MASS-1 and UQAC-FeS-1).

Figure S3. Trace element associated with apatite from sample HN99-46.

Figure S4. Mantle-normalised multi-element diagram for apatite trace elements extracted from the new mapping protocol (this work) and compared with previous laser work on the same thin section (Tollari *et al.* 2008, Kieffer *et al.* 2022).

Figure S5. Trace element distribution associated with ilmenite (sample HN99-46).

Figure S6. Trace elements preferentially hosted within titanomagnetite in sample HN99-46.

Figure S7. Trace elements associated with pyrite in sample HN99-46.

Figure S8. Close-up view of pyrite from the late-stage vein in HN99-46 revealing complex Co, Ni, Cu, Pb and Tl zonation.

Figure S9. Trace elements in HN99-46 that are highly incompatible into the six major phases.

Appendix S1. Discussion of (1) ablation mode and beam shape and (2) quality control. (3) Quantification of trace elements in sample HN-99-46.

Table S1. List of reference materials used to calibrate and monitor the new multi-phase mapping protocol.

Table S2. Measurement results for analysed reference materials.

Table S3. Details results of lower limits of detection (LLoD), upper limits of detection (ULoD), and LLoD comparison with LA-Q-ICP-MS.

Table S4. Comparison of the measured trace elements in ilmenite and titanomagnetite in sample HN99-46 with previously published data (Méric 2011).

Table S5. Extended list of minerals and their total effective yield (TEY) relative to the Type-A natural magnetite (HN99-46).

This material is available from: http://onlinelibrary.wiley.com/doi/10.1111/ggr.12482/abstract (This link will take you to the article abstract).